

1 An Emerging Aerosol Climatology via Remote Sensing over Metro Manila, Philippines

2  
3 Genevieve Rose Lorenzo<sup>1,2</sup>, Avelino F. Arellano<sup>1</sup>, Maria Obiminda Cambaliza<sup>2,3</sup>, Christopher  
4 Castro<sup>1</sup>, Melliza Templonuevo Cruz<sup>2,4</sup>, Larry Di Girolamo<sup>5</sup>, Glenn Franco Gacal<sup>2</sup>, Miguel  
5 Ricardo A. Hilario<sup>1</sup>, Nofel Lagrosas<sup>6</sup>, Hans Jarett Ong<sup>2</sup>, James Bernard Simpas<sup>2,3</sup>, Sherdon Niño  
6 Uy<sup>2</sup>, and Armin Sorooshian<sup>1,7</sup>

7  
8 <sup>1</sup>Department of Hydrology and Atmospheric Sciences, University of Arizona, Tucson, Arizona,  
9 85721, USA

10 <sup>2</sup>Air Quality Dynamics-Instrumentation & Technology Development Laboratory, Manila  
11 Observatory, Quezon City, 1108, Philippines

12 <sup>3</sup>Department of Physics, School of Science and Engineering, Ateneo de Manila University,  
13 Quezon City, 1108, Philippines

14 <sup>4</sup>Institute of Environmental Science and Meteorology, University of the Philippines, Diliman,  
15 Quezon City, 1101, Philippines

16 <sup>5</sup>Department of Atmospheric Science, University of Illinois, Urbana-Champlain, Illinois, 61801,  
17 USA

18 <sup>6</sup>Center for Environmental Remote Sensing, Chiba University, Chiba, 263-8522, Japan

19 <sup>7</sup>Department of Chemical and Environmental Engineering, University of Arizona, Tucson,  
20 Arizona, 85721, USA

21  
22 *Correspondence to:* armin@arizona.edu

23 **Abstract**

24 Aerosol particles in Southeast Asia are challenging to characterize due to their complex life cycle  
25 within the diverse topography and weather in the region. An emerging aerosol climatology was  
26 established based on AERONET data (December 2009 to October 2018) for clear sky days in  
27 Metro Manila, Philippines. Aerosol optical depth (AOD) values were highest from August to  
28 October, partly from fine urban aerosol particles, including soot, coinciding with the burning  
29 season in Insular Southeast Asia when smoke is often transported to Metro Manila during the  
30 southwest monsoon. Clustering of AERONET volume size distributions (VSD) resulted in five  
31 aerosol particle sources based on the position and magnitude of their peaks in the VSD and the  
32 contributions of specific particle species to AOD per cluster based on MERRA-2. The clustering  
33 showed that the majority of aerosol particles above Metro Manila were from a clean marine  
34 source (58%), which could be related to AOD values there being relatively smaller than in other  
35 cities in the region. The following are the other particle sources over Metro Manila: fine polluted  
36 (20%), mixed dust (12%), urban/industrial (5%), and cloud processing (5%). Furthermore,  
37 MERRA-2 AOD data over Southeast Asia were analyzed using empirical orthogonal functions.  
38 Along with AOD fractional compositional contributions and wind regimes, four dominant  
39 aerosol particle air masses emerged: two sulfate air masses from East Asia, an organic carbon  
40 source from Indonesia, and a sulfate source from the Philippines. Knowing the local and regional  
41 aerosol particle air masses that impact Metro Manila is useful in identifying the sources while  
42 gaining insight on how aerosol particles are affected by long-range transport and their impact on  
43 regional weather.

## 44 1. Introduction

45 Although Southeast Asia is one of the most rapidly developing regions in the world with a  
46 growing number of extensive research conducted (Reid et al., 2023), there remain knowledge  
47 gaps related to aerosol particles in the area (Tsay et al., 2013; Lee et al., 2018; Chen et al., 2020;  
48 Amnuaylojaroen, 2023). The region represents a complex geographic, meteorological, and  
49 hydrological environment making it challenging to understand aerosol particle characteristics,  
50 especially interactions between aerosol particles with their environment (Reid et al., 2013). The  
51 island of Luzon in the Philippines in particular is very populated and is characterized by high  
52 levels of anthropogenic emissions superimposed on natural emissions from the surrounding  
53 waters (AzadiAghdam et al., 2019) and long-range transport of emissions from areas such as  
54 Indonesia and East Asia (Braun et al., 2020; Hilario et al., 2020a; Hilario et al., 2020b; Hilario et  
55 al., 2021a). Aerosol particle lifecycle in the region is impacted by Philippine weather that is  
56 marked by two distinct monsoons, typhoons, the intertropical convergent zone, and impacts from  
57 El Niño-Southern Oscillation and Madden-Julian Oscillation (Cruz et al., 2013; Xian et al., 2013;  
58 Reid et al., 2012; Reid et al., 2015; Hilario et al., 2021b). Studying this area is informative owing  
59 to the wide dynamic range in aerosol particle and weather conditions, which are interconnected.  
60 The overlapping of large fraction of cirrus clouds with lower clouds in the area (Hong and Di  
61 Girolamo, 2020) makes space-borne remote sensing of aerosol particles very challenging (Reid  
62 et al., 2013; Lin et al., 2014). These reasons motivated the NASA Cloud, Aerosol, and Monsoon  
63 Processes Philippines Experiment (CAMP<sup>2</sup>Ex) airborne measurement campaign in 2019 to  
64 understand the interaction between tropical meteorology and aerosol particles (Di Girolamo et  
65 al., 2015; Reid et al., 2023). However, those short terms measurements cannot provide an  
66 adequate assessment of aerosol behavior across all seasons and over many years.

67 The NASA AErosol RObotic NETwork (AERONET) (Holben et al., 1998) is pivotal in  
68 providing broad temporal coverage of aerosol characteristics in specific locations with a column-  
69 based perspective from the ground up. Aerosol climatology studies in different regions have  
70 proved beneficial to understand temporal characteristics of aerosol particle concentrations and  
71 properties, in addition to identifying potential source regions along with interactions with clouds  
72 and rainfall (Stevens and Feingold, 2009; Li et al., 2011; Tao et al., 2012; Crosbie et al., 2014;  
73 Kumar et al., 2015; Alizadeh-Choobari and Gharaylou, 2017; Mora et al., 2017; Aldhaif et al.,  
74 2021). To our knowledge, there has not been a remote sensing-based aerosol climatology study  
75 for the Metro Manila region of Luzon, which has approximately 16 cities, a population of 12.88  
76 million, and a high population density of 20,800 km<sup>-2</sup> (PSA, 2016; Alas et al., 2018).

77 Most of the past studies involving long-term remotely sensed aerosol particle data in Southeast  
78 Asia (Cohen, 2014; Nakata et al., 2018; Nguyen et al., 2019b) had no specific focus on the  
79 Philippines. The Philippines is considered as part of the Maritime Continent (MC), the island  
80 nations sub-region of Southeast Asia. The other Southeast Asia sub-region, Peninsular Southeast  
81 Asia (PSEA), comprises those nations within the continental Asia land mass. These two regions  
82 have separate aerosol sources and climate, where MC is dependent on the intertropical  
83 convergent zone (ITCZ) and PSEA is dependent on both the ITCZ and monsoon systems (Dong  
84 and Fu, 2015). Only the southern part of the Philippines is climatologically part of MC (Ramage,  
85 1971), however, and northwest Philippines, where Metro Manila is located, is affected by the  
86 monsoons and tropical cyclones aside from the ITCZ (Chang et al., 2005; Yumul Jr et al., 2010;  
87 Bagtasa, 2017). These unique meteorological influences and extensive local aerosol particle

88 sources warrant a unique aerosol climatology over Metro Manila, one of a polluted source in a  
 89 tropical marine environment, and its effects on cloud formation in the area. Aerosol effects on  
 90 clouds in the marine environment are associated with the largest uncertainties in climate change  
 91 research (Hendrickson et al., 2021; Wall et al., 2022) and the Philippines was ranked as the 5th  
 92 country globally as most at risk to climate change and extreme weather from 1997 to 2018  
 93 (Eckstein et al., 2018). There have been several surface measurements of aerosol particles made  
 94 in Metro Manila for the past 20 years (Oanh et al., 2006; Bautista VII et al., 2014; Cruz et al.,  
 95 2019) but columnar ground-based measurements there are just beginning to be established  
 96 (Dorado et al., 2001; Ong et al., 2016; Cruz et al., 2023). The AERONET sun photometer is one  
 97 of the first long-term column-based aerosol instruments in Metro Manila and the Philippines  
 98 (Ong et al., 2016).

99 The goal of this study is to use multi-year AERONET data in Manila Observatory along with  
 100 other complementary datasets (MERRA-2, PERSIANN, MISR, HYSPLIT, and NAAPS) to  
 101 address the following questions: (1) what are the monthly characteristics of aerosol particles over  
 102 Metro Manila, Philippines?; (2) what are the possible sources and factors influencing the  
 103 observed characteristics?; (3) what relationships are evident between aerosol particles and cloud  
 104 characteristics?; and (4) what are the regional and local aerosol particle air masses that influence  
 105 Metro Manila?

106

## 107 2. Methods

108 This work relies on analysis of several datasets summarized in Table 1 and the following  
 109 subsections. The common time range used for all datasets is between January 2009 and October  
 110 2018.

111 **Table 1:** Summary of datasets over Metro Manila used in this work covering the period from  
 112 January 2009 to October 2018.

Parameter	Data Source	Spatial Coverage	Time Coverage
Aerosol Optical Depth (500 nm)	AERONET	14.635°N, 121.078°E	Jan 2009 - Oct 2018
Asymmetry Factor (440 nm - 1020 nm)	AERONET	14.635°N, 121.078°E	Jan 2009 - Oct 2018
Extinction Angstrom Exponent (440 nm -870 nm)	AERONET	14.635°N, 121.078°E	Jan 2009 - Oct 2018
Fine Mode Fraction	AERONET	14.635°N, 121.078°E	Jan 2009 - Oct 2018
Precipitable Water	AERONET	14.635°N, 121.078°E	Jan 2009 - Oct 2018
Single Scattering Albedo (440 nm - 1020 nm)	AERONET	14.635°N, 121.078°E	Jan 2009 - Oct 2018
Refractive Index (Real and Imaginary; 440 nm - 1020 nm)	AERONET	14.635°N, 121.078°E	Jan 2009 - Oct 2018
Volume Size Distribution	AERONET	14.635°N, 121.078°E	Jan 2009 - Oct 2018
Low Cloud Fraction (MODIS)	MERRA-2	14.3°N - 14.8°N, 120.75°E - 121.25°E	Jan 2009 - Dec 2018
Planetary Boundary Layer Height	MERRA-2	14.3°N - 14.8°N, 120.75°E - 121.25°E	Jan 2009 - Dec 2018

Relative Humidity (975 mb)	MERRA-2	14.3°N - 14.8°N, 120.75°E - 121.25°E	Jan 2009 - Dec 2018
Sea Level Pressure	MERRA-2	14.3°N - 14.8°N, 120.75°E - 121.25°E	Jan 2009 - Dec 2018
Temperature (975 mb)	MERRA-2	14.3°N - 14.8°N, 120.75°E - 121.25°E	Jan 2009 - Dec 2018
Wind (975 mb)	MERRA-2	14.3°N - 14.8°N, 120.75°E - 121.25°E	Jan 2009 - Dec 2018
Total Extinction Aerosol Optical Depth (550 nm)	MERRA-2	14.3°N - 14.8°N, 120.75°E - 121.25°E	Jan 2009 - Dec 2018
Sulfate, Black Carbon, Organic Carbon, Dust, and Sea Salt Extinction Aerosol Optical Depth (550 nm)	MERRA-2	14.3°N - 14.8°N, 120.75°E - 121.25°E	Jan 2009 - Dec 2018
Precipitation	PERSIANN	14.3°N - 14.8°N, 120.75°E - 121.25°E	Jan 2009 - Dec 2018

## 113 2.1 Datasets

### 114 2.1.1 AERONET

115 The central dataset used is that of sun photometer measurements and derived (inversion)  
116 parameters from the AERONET (Holben et al., 1998) site at the Manila Observatory in Quezon  
117 City, Philippines (14.64°N, 121.08°E, ~70 m. a. s. l.). Direct sunlight extinction measurements  
118 were made at nominal wavelengths of 340, 380, 440, 500, 675, 870, 940, and 1020 nm, from  
119 which aerosol optical depth (AOD) was calculated (except for 940 nm, which is for water vapor)  
120 (Eck et al., 2013). AOD is a commonly used proxy for aerosol particle loading in the air column  
121 from the ground up (Holben et al., 2001); higher AOD translates to more aerosol particle  
122 extinction in the column above a location. The extinction angstrom exponent (EAE) and the fine  
123 mode fraction (FMF) are also AERONET direct sun products that are retrieved after the  
124 application of a spectral de-convolution algorithm (O'Neill et al., 2003). For the inversion  
125 products, it is through radiative retrievals that the volume size distribution (VSD) and complex  
126 refractive index (RI) are gathered and from which single scattering albedo (SSA) and asymmetry  
127 factor (AF) are calculated. The AERONET observations were made during clear sky conditions,  
128 which has been shown (Hong and Di Girolamo, 2022) to be able to represent all sky conditions.

129 For the inversions, four wavelengths (440, 670, 870, and 1020 nm) of the radiometer spectral  
130 channels were chosen for diffuse radiance measurements and to avoid gas absorption (Dubovik  
131 et al., 1998). Version 3 Direct Sun and Inversion algorithms (AERONET, 2019; Giles et al.,  
132 2019) were used with the Almuqantar Sky Scan Scenario to derive the following parameters with  
133 level 2.0 (automatically cloud-cleared and quality controlled datasets with pre- and post-field  
134 calibrations) data quality: column AOD (500 nm), fine mode fraction (500 nm), extinction  
135 angstrom exponent (440 – 870 nm), precipitable water (940 nm), single scattering albedo (440,  
136 670, 870, and 1020 nm), asymmetry factor (440, 670, 870, and 1020 nm), refractive index (440,  
137 670, 870, and 1020 nm), and VSD. The version 3 products are able to keep fine mode aerosol  
138 particle data (haze and smoke) as well as remove optically thin cirrus clouds in order to retain  
139 more aerosol particle measurements in the database (Giles et al., 2019). Cloud screening in the  
140 version 3 product improves remote sensing measurements in Southeast Asia in general, where  
141 cirrus clouds are pervasive (Reid et al., 2013). At most, a total of 29,037 direct sun and 1419  
142 inversion AERONET daytime data points were available between January 2009 and October  
143 2018.

### 144 2.1.2 MERRA-2

145 Modern Era-Retrospective Analysis for Research and Applications, Version 2 (MERRA-2:  $0.5^\circ$   
146  $\times 0.625^\circ$  approximate resolution) meteorological and aerosol particle composition reanalysis data  
147 (Bosilovich, 2016; Gelaro et al., 2017; Randles et al., 2017) were acquired for the area around  
148 Manila Observatory ( $14.25^\circ\text{N} - 14.75^\circ\text{N}$ ,  $120.9375^\circ\text{E} - 121.5625^\circ\text{E}$ ). The aerosol reanalysis  
149 data includes data assimilation of AOD from the Moderate Resolution Imaging  
150 Spectroradiometer (MODIS: Terra, 2000 to present and Aqua, 2002 to present), Advanced Very  
151 High Resolution Radiometer (AVHRR, 1979-2002), and Multiangle Imaging SpectroRadiometer  
152 (MISR, 2000-2014) (Buchard et al., 2017; Rizza et al., 2019). The following products were used:  
153 M2I3NPASM Assimilated Meteorological Fields (3-hourly) for 975 mb level winds,  
154 temperature, relative humidity, and sea level pressure; M2T1NXFLX Surface Flux Diagnostics  
155 (1-hourly from 00:30 UTC time-averaged) 2D for planetary boundary layer height;  
156 M2T1NXCSP COSP Satellite Simulator (1-hourly from 00:30 UTC time-averaged) for MODIS  
157 mean low cloud fraction (cloud top pressure  $> 680$  hPa); and M2T1NXAER Aerosol Diagnostics  
158 (1-hourly from 00:30 UTC time-averaged) for Total AOD and speciated AOD (Sulfate, Black  
159 Carbon (BC), Organic Carbon (OC), Dust, and Sea Salt).

160 MERRA-2 meteorological and aerosol particle composition monthly mean reanalysis data  
161 (Bosilovich, 2016; Gelaro et al., 2017; Randles et al., 2017) were also acquired for a larger  
162 region ( $30^\circ \times 30^\circ$ ), the Southeast Asia region ( $0^\circ\text{N} - 30^\circ\text{N}$ ,  $105^\circ\text{E} - 135^\circ\text{E}$ ) for the period from  
163 2009 to 2018. This is within the spatial domain of the CAMP<sup>2</sup>Ex airborne measurement  
164 campaign which, as mentioned earlier, targets the interaction between tropical meteorology and  
165 aerosol particles. The following datasets ( $0.5^\circ$  latitude and  $0.625^\circ$  longitude resolution) were  
166 used: MERRA-2 tavgM\_2d\_aer\_Nx: Aerosol Assimilation (M2TMNXAER) for Total 500 nm  
167 AOD and speciated 500 nm AOD (Sulfate, BC, OC, Dust, and Sea Salt) and MERRA-2  
168 instM\_3d\_ana\_Np: Analyzed Meteorological Fields (M2IMNPANA) for 1000 hPa and 725 hPa  
169 level U and V winds. The total MERRA-2 AOD for the region (mean over  $30^\circ \times 30^\circ$  region) was  
170 used along with MISR AOD data (mean over  $30^\circ \times 30^\circ$  region) to assess the influence of long-  
171 range sources to the aerosol column over Manila Observatory. The monthly meteorological and  
172 aerosol particle composition data for the region will be used for empirical orthogonal functions,  
173 which will be described later.

### 174 2.1.3 PERSIANN

175 Hourly precipitation data were obtained from the Precipitation Estimation from the Remotely  
176 Sensed Information using Artificial Neural Networks (PERSIANN) database of the Center for  
177 Hydrometeorology and Remote Sensing (CHRS) at the University of California, Irvine (UCI).  
178 Hourly data were accumulated for running three-day totals, which were compared to AERONET  
179 data. The data were averaged between the four grids that included the area of interest as well as  
180 ensuring a similar spatial domain ( $14.5^\circ\text{N} - 15.0^\circ\text{N}$ ,  $120.75^\circ\text{E} - 121.25^\circ\text{E}$ ) to the MERRA-2  
181 dataset.

### 182 2.1.4 MISR

183 Monthly 500 nm AOD data (Level 3 Global Aerosol:  $0.5^\circ \times 0.5^\circ$  spatial resolution in the region  
184  $0.25^\circ\text{N} - 30.25^\circ\text{N}$  and  $104.75^\circ\text{E} - 134.75^\circ\text{E}$ ) from 2009 to 2018 are used from the Multi-angle  
185 Imaging SpectroRadiometer (MISR), (Diner et al., 2007; Garay et al., 2018) as regional  
186 (Southeast Asia) baseline remote sensing data to support the Manila Observatory AERONET  
187 data. The regional ( $30^\circ \times 30^\circ$ ) MISR data was used to confirm regional sources of aerosols that  
188 may be influencing the AOD over Metro Manila. Level 3 MISR products are global maps of

189 parameters available in Level 2 (measurements derived from the instrument data) products.  
190 MISR is ideal for remote sensing in the CAMP<sup>2</sup>Ex region because it has an overpass at 10:30  
191 AM ECT (descending mode) (when cirrus is minimal) and its retrievals have been shown to be  
192 unimpacted by small cumulus (Zhao et al., 2009), which are typical in the region. MISR has  
193 relatively more accurate AOD and agrees better with AERONET data compared to other satellite  
194 products due to its multi-angle measurements (Choi et al., 2019; Kuttippurath and Raj, 2021).  
195 The MISR sampling noise is relatively small due to the large domain and seasonal averages that  
196 are considered in this study. MISR is also the only passive sensor that speciates aerosol particle  
197 size and shape. All these factors led to the choice of using regional MISR data to associate long-  
198 range sources influencing AERONET data in Manila Observatory. Monthly mean AOD (bin 0)  
199 were extracted for Southeast Asia (0.25°N – 30.25°N, 104.75°E – 134.75°E) within the  
200 CAMP<sup>2</sup>Ex region. Monthly mean AOD values were then calculated for each 0.5° grid point and  
201 then for the 30° × 30° region, where the standard error in the monthly mean for the region is less  
202 than 0.002. MISR monthly mean time series of size, shape, and absorption speciated 550 nm  
203 AOD and angstrom exponent in the CAMP<sup>2</sup>Ex domain (6.5°N – 22.5°N, 116.5°E – 128.5°E;  
204 March 2000 to December 2020) are also used to support the findings from the AERONET data.

#### 205 2.1.5 NAAPS

206 Archived maps of total and speciated optical depths and surface concentrations of sulfate, dust,  
207 and smoke for Southeast Asia are used from the Navy Aerosol Analysis and Prediction System  
208 (NAAPS: 1° × 1° spatial resolution) (Lynch et al., 2016), and which are publicly available at  
209 <https://www.nrlmry.navy.mil/aerosol/>. This reanalysis product relies on the Navy Global  
210 Environmental Model (NAVGEM) for meteorological fields (Hogan et al., 2014). Hourly maps  
211 were downloaded for aerosol particle events of interest based on AERONET data. These maps  
212 help associate possible regional emission sources to extreme aerosol loading events in Manila  
213 Observatory. Previous studies have used NAAPS data for an overview of aerosol sources in  
214 specific regions of interest (Ross et al., 2018; Foth et al., 2019; Markowicz et al., 2021; Harenda  
215 et al., 2022; Mims III, 2022). More recent studies show the need to improve aerosol  
216 representation in NAAPS (Edwards et al., 2022), so we will use NAAPS qualitatively, together  
217 with MERRA-2 compositional AOD data and back-trajectories, for an overview of aerosol  
218 sources that may contribute to extreme events with high AOD from AERONET.

#### 219 2.1.6 HYSPLIT

220 Back-trajectories from the National Oceanic and Atmospheric Administration’s (NOAA) Hybrid  
221 Single-Particle Lagrangian Integrated Trajectory (HYSPLIT) model (Stein et al., 2015; Rolph et  
222 al., 2017) were used to provide support for the AERONET monthly aerosol characteristics and  
223 the chosen case studies. Three and seven-day back-trajectories with six-hour resolution were  
224 generated based on the NCEP/NCAR reanalysis meteorological dataset and with a resolution of  
225 1° and a vertical wind setting of “model vertical velocity”. The three-day data were used to map  
226 the density of trajectories reaching Manila Observatory in each month from 2008 to 2019. The  
227 seven-day data were used in the analysis of the case studies. Trajectories were computed for an  
228 end point with an altitude of 500 m above ground level at the Manila Observatory. This altitude  
229 represents the mixed layer based on related surface air quality studies (Crosbie et al., 2014; Mora  
230 et al., 2017; Schlosser et al., 2017; Aldhaif et al., 2020), including a previous study for the same  
231 area (Stahl et al., 2020).

#### 232 2.1.7 NASA Worldview

233 Archived maps of cloud fraction (Aqua MODIS and Terra MODIS) over Metro Manila and  
 234 Southeast Asia were downloaded from NASA Worldview (<https://worldview.earthdata.nasa.gov>)  
 235 for events of interest based on AERONET data.  
 236

## 237 2.2 Clustering

238 Available AERONET VSD data (0.050  $\mu\text{m}$  to 15.000  $\mu\text{m}$  particle radius in 22 logarithmically  
 239 equidistant discrete points, 1419 data points) were clustered via k-means clustering (Lloyd,  
 240 1982). The algorithm used was k-means++ (Arthur and Vassilvitskii, 2006). The ideal number  
 241 of clusters was chosen based on relatively highest ( $>0.5$ ) average silhouette value and the  
 242 presence of a cluster with a second peak in the larger accumulation mode of the VSD. The  
 243 clusters were analyzed based on their associated meteorological conditions and aerosol particle  
 244 characteristics and were classified into air mass types (Table 2) based on estimates from previous  
 245 studies (Dubovik et al., 2002; Pace et al., 2006; Kaskaoutis et al., 2007; Kaskaoutis et al., 2009;  
 246 Sorooshian et al., 2013; Kumar et al., 2014; Sharma et al., 2014; Che et al., 2015; Kumar et al.,  
 247 2015; Deep et al., 2021). The first four mentioned air mass types in Table 2 are the most general,  
 248 and four more classifications based on aerosol particle sources are included. The urban/industrial  
 249 air mass type here refers to local combustion along with long-range transported biomass burning  
 250 (Kaskaoutis et al., 2009). While these classifications are not rigid definitions of air masses, they  
 251 help in understanding the sources that contribute to aerosols in Metro Manila and in identifying  
 252 cases where certain sources are more influential than others.

253 **Table 2:** Summary of threshold values of aerosol optical depth (AOD), angstrom exponent (AE),  
 254 fine mode fraction (FMF), and single scattering albedo (SSA) used to identify air mass types.

Air Mass Type	AOD	AE	FMF	SSA	Source
Clean Fine	$< 0.1^a$	$> 1^a$	$> 0.7^a$	-	Sorooshian et al., 2013
Polluted Fine	$> 0.1^a$	$> 1^a$	$> 0.7^a$	-	Sorooshian et al., 2013
Clean Coarse	$< 0.1^a$	$< 1^a$	$< 0.3^a$	-	Sorooshian et al., 2013
Polluted Coarse	$> 0.1^a$	$< 1^a$	$< 0.3^a$	-	Sorooshian et al., 2013
Clean Marine	$< 0.2^b$	$< 0.9^d$	-	0.98 <sup>e</sup>	Kaskaoutis et al., 2009 Dubovik et al., 2002
Urban/Industrial	$> 0.2^b$	$> 1^d$	-	0.9- 0.98 <sup>e</sup>	Kaskaoutis et al., 2009 Dubovik et al., 2002
Biomass Burning	-	$> 1.4^a$	-	0.89- 0.95 <sup>e</sup>	Deep et al., 2021 Dubovik et al., 2002 Kaskaoutis et al., 2009
Desert Dust	$> 0.3^c$	$< 1^d$	-	0.92- 0.93 <sup>e</sup>	Deep et al., 2021 Dubovik et al., 2002

<sup>a</sup> from MODIS  
<sup>b</sup> AOD at 500 nm  
<sup>c</sup> AOD at 400 nm  
<sup>d</sup> AE at 380 nm to 870 nm  
<sup>e</sup> SSA at 440 nm

255



256 **2.3 Extreme Event Analysis**

257 Aerosol particle events based on the three clusters with the highest VSD concentrations were  
258 identified to characterize different types of sources and processes impacting aerosol particle  
259 columnar properties above Metro Manila. The three events are described below.

260 **2.3.1 Smoke Long Range Transport**

261 Events related to transported biomass burning/smoke were chosen from the AERONET VSD  
262 data that were clustered as urban/industrial (with a dominant submicrometer peak) (Eck et al.,  
263 1999) over Metro Manila. Cases with the highest black carbon contribution to total AOD from  
264 the MERRA-2 dataset were considered. Maps from NAAPS of high smoke contributions to  
265 AOD and surface smoke contributions in the direction of back-trajectories HYSPLIT were used  
266 to provide support for the likely source and transport pathway for the smoke cases.

267 **2.3.2 Dust Long Range Transport**

268 A dust transport case over Metro Manila was identified from the AERONET VSD dust cluster  
269 (with an enhanced coarse peak in the AERONET VSD compared to the submicrometer fraction)  
270 (Eck et al., 1999), the highest dust contribution to AOD from the MERRA-2 dataset, and high  
271 dust contributions to AOD from NAAPS. Surface dust concentrations from NAAPS along the  
272 HYSPLIT back-trajectories improved the plausibility of dust for this case.

273 **2.3.3 Cloud Processing**

274 Cloud processing events were identified based on bimodal submicrometer VSDs (Eck et al.,  
275 2012) and a relatively large sulfate contribution to AOD over Metro Manila from the MERRA-2  
276 dataset, since this species is predominantly produced via cloud processing (Barth et al., 2000;  
277 Faloon, 2009). The presence of clouds was verified qualitatively with MODIS (Aqua and Terra)  
278 imagery from NASA Worldview in the path of air parcels reaching Metro Manila based on  
279 HYSPLIT back-trajectories.

280

281 **2.4 Empirical Orthogonal Functions**

282 Regional analysis of aerosol particles in Southeast Asia and Asia in general show the prevalence  
283 of biomass burning in the region, as well as the larger influence of anthropogenic emissions in  
284 East Asia (Nakata et al., 2018). These large prevalent sources may overshadow other relevant but  
285 weaker sources in the region, such as local sources. Due to the complex nature of aerosol  
286 particles, analysis techniques such as principal component analysis and clustering along with  
287 recent improvements in gridded datasets help detect spatial and temporal patterns that would  
288 otherwise be difficult to make with noise interference and even weak signals (Li et al., 2013;  
289 Sullivan et al., 2017; Plymale et al., 2021). Understanding the dominant air masses around  
290 Southeast Asia will help in distinguishing local and transported particles that influence the  
291 aerosol climatology in Metro Manila.

292 To contextualize the analysis of aerosol particle masses in Metro Manila, major regional sources  
293 of aerosol particles in Southeast Asia were identified based on the dominant principal  
294 components from empirical orthogonal (EOF) analysis of AOD. EOF analysis was done on the  
295 monthly AOD data (January 2009 to December 2018) from MERRA-2 for the Southeast Asia  
296 region for the months similar in scope to the AERONET data. EOF analysis needs a complete

297 dataset with no data gaps, which is not available with pure satellite retrievals like MISR; the  
298 MERRA-2 reanalysis dataset alleviates this issue.

299 The monthly MERRA-2 AOD maps ( $0^{\circ}$  -  $30^{\circ}$ N,  $105^{\circ}$ E –  $135^{\circ}$ E with  $0.5^{\circ}$  latitude and  $0.625^{\circ}$   
300 longitude resolution) (Lat: 61 rows x Lon: 49 columns) for the Southeast Asia region (presented  
301 subsequently) were first deseasonalized. Then, the AOD anomaly per grid per year (of the 120  
302 months) was calculated by subtracting the monthly mean AOD from each value of a given month  
303 (Li et al., 2013). The anomalies per grid were weighted depending on their latitude by  
304 multiplying the anomalies by the square root of the cosine of their latitudes.

305 EOF, specifically singular value decomposition (SVD), analysis (Björnsson and Venegas, 1997)  
306 was then performed. To prepare the data for the analysis, they were transformed such that the  
307 final matrix was a 2D matrix (120 x 2989) with each row representing a year, and each column  
308 representing a grid in the map. The matrix was analyzed for eigenvalues using SVD in Matlab,  
309 which outputs the eigenvalue (S) and eigenvector (U: principal components and V: empirical  
310 orthogonal functions) matrices. The eigenvalues were, by default, arranged in descending order.  
311 Each PC time series was standardized by dividing each PC value by the standard deviation per  
312 PC time series (120 months).

313 An eigenvalue spectrum was also plotted based on the variance explained by each eigenvalue  
314 and error bars that were calculated using the North test (North et al., 1982). Then, the  
315 unweighted AOD anomalies were regressed onto the first three standardized PCs. Each grid  
316 therefore had a regression between 120 pairs (unweighted AOD anomalies vs standardized PCs).  
317 From the linear regression equation, the regression coefficient per grid was calculated. Each grid  
318 on the Southeast Asia map was colored based on the calculated regression coefficient value.

## 319 **2.5 Correlations**

321 The first three standardized PCs of AOD anomalies were correlated to deseasonalized  
322 compositional AOD fractions (Sulfate, BC, OC, Dust, and Sea Salt). For each correlation, the t-  
323 test value was calculated, and the resulting t-score was compared to a t-critical value for  $\sim n=100$   
324 pairs (n is the number of pairs of data, in this case 120 months) for 0.90 confidence level, which  
325 is 1.660. Correlations that have t-values exceeding +1.660 or less than -1.660 (two-tailed test) are  
326 significant (90% confidence).

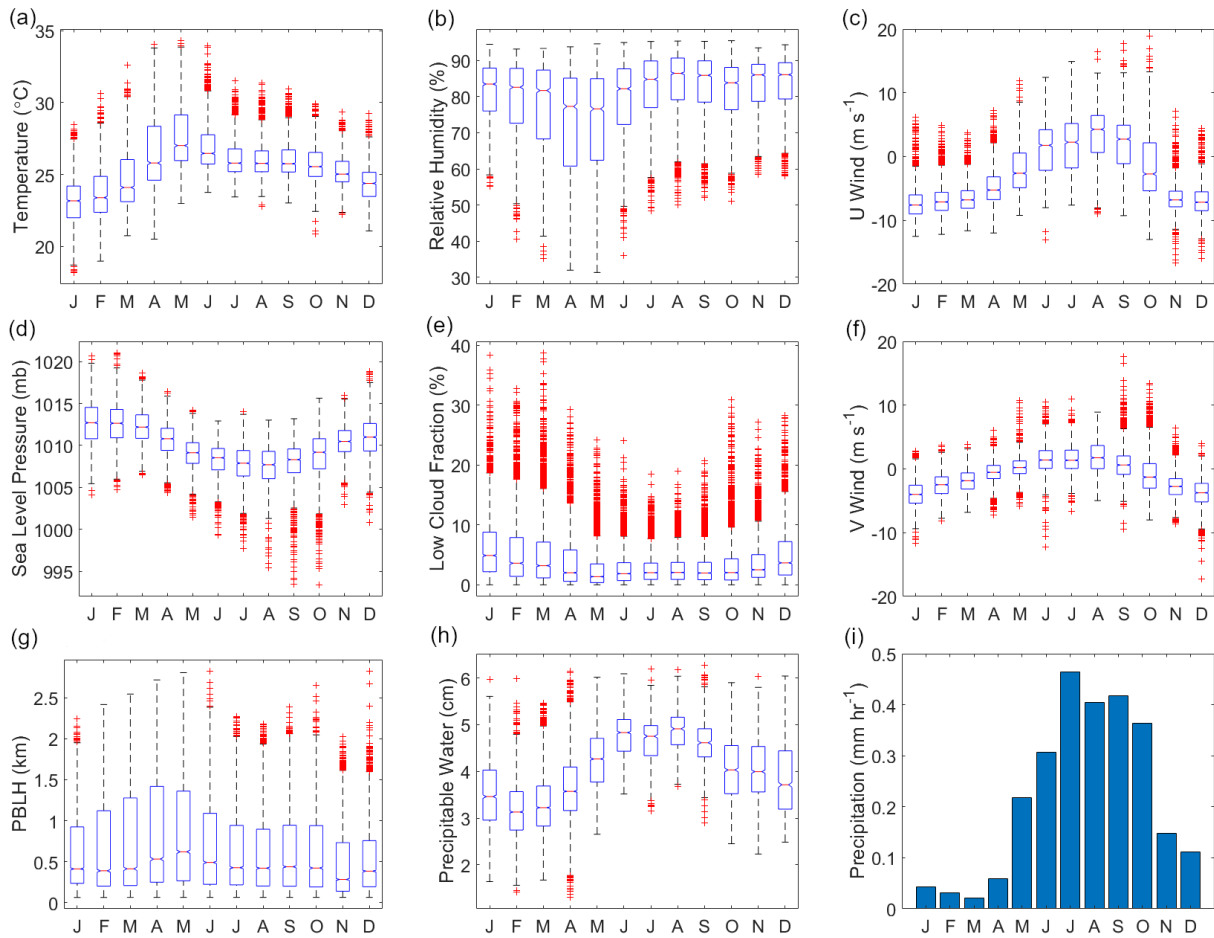
327

## 328 **3 Results and Discussion**

### 329 **3.1 Meteorology and Atmospheric Circulation**

330 Knowledge of monthly behavior of weather in the study region helps interpretation of aerosol  
331 particle data. Philippine climate is influenced both by the winter northeast monsoon  
332 ( $\sim$ November to April, Amihan) and the summer southwest monsoon ( $\sim$ May to October, Habagat)  
333 (Coronas, 1920; Flores, 1969; Matsumoto et al., 2020). Median 3-hourly temperatures at 975 mb  
334 per month (MERRA-2, 975 mb) (Fig. 1a) ranged from  $23.2^{\circ}$  C in January during the winter  
335 northeast monsoon, to  $27.0^{\circ}$  C in May during the transition from the summer season, as defined  
336 in (Bañares et al., 2021), to the southwest monsoon. May was also the month with the lowest  
337 median 3-hourly relative humidity (76.6%) (MERRA-2, 975 mb) (Fig. 1b). The highest median  
338 level of relative humidity at 975 mb for a month was in August (86.5 %) during the summer  
339 southwest monsoon, which is also the time of the year (June to August) when rainfall peaks in

340 the region where the sampling station (Manila Observatory) is located (Coronas, 1920; Cruz et  
 341 al., 2013). The highest mean hourly precipitation (Fig. 1i) per month was from July (0.46 mm hr<sup>-1</sup>)  
 342 to September (0.42 mm hr<sup>-1</sup>), while March exhibited the lowest mean hourly rainfall (0.02 mm  
 343 hr<sup>-1</sup>). Like relative humidity and precipitation, median precipitable water (from available  
 344 AERONET data of 513 points in August, 4015 points in February, and 5049 points in March)  
 345 (Fig. 1h) was highest in August (4.9 cm) and lowest in February and March (3.1 cm and 3.2 cm,  
 346 respectively).  
 347

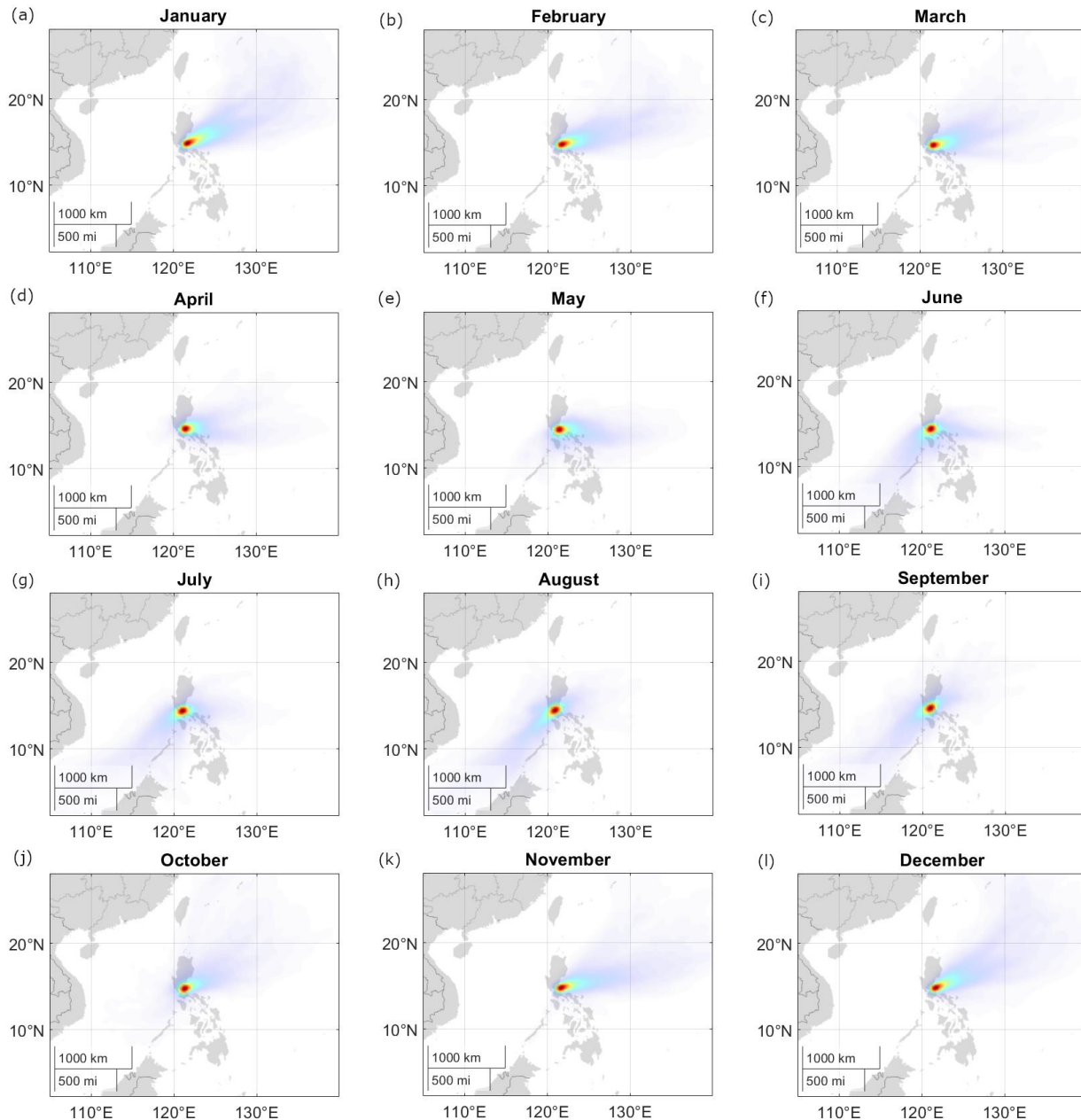


348  
 349 **Figure 1:** Monthly characteristics of meteorological parameters for Metro Manila, Philippines  
 350 based on data between January 2009 and October 2018. MERRA-2 parameters: (a) temperature  
 351 at 975 mb, (b) relative humidity at 975 mb, (c/f) u and v wind at 975 mb, (d) sea level pressure,  
 352 (g) planetary boundary layer height (PBLH), (e) low cloud fraction (cloud top pressure > 680  
 353 hPa); AERONET: (h) precipitable water (data counts per month Jan: 2131, Feb: 4015, Mar:  
 354 5049, Apr: 5844, May: 3448, Jun: 1696, Jul: 652, Aug: 513, Sep: 753, Oct: 1700, Nov: 2084,  
 355 Dec: 1449); PERSIANN: (i) mean hourly precipitation per month.  
 356  
 357

358 The lowest 3-hourly median pressures (MERRA-2) were observed (Fig. 1d) between July and  
 359 September during the southwest monsoon season (~985.2 – 985.8 mb). This is also the time  
 360 when the most number of tropical cyclones pass the island of Luzon (Wu and Choy, 2016). The

361 highest 3-hourly median pressures (988.1 – 990.0 mb) were during the winter northeast  
362 monsoon.

363 Median winds (MERRA-2) were from the south/southwest direction from June to September  
364 (Fig. 1c and 1f), associated with the summer southwesterly monsoon. HYSPLIT back-  
365 trajectories show the same wind pattern (Fig. 2f to 2i). The highest median 3-hourly wind speeds  
366 (MERRA-2) (Fig. 1c and 1f) during the southwest monsoon were recorded for August (u: 4.2 m  
367  $s^{-1}$  and v: 1.7 m  $s^{-1}$ ). Median winds begin to transition in October and November (to the northeast  
368 monsoon: Amihan) (Fig. 2j and 2k) coming from the east/northeast and maintained until  
369 February (Fig. 2b), which is towards the end of the winter northeast monsoon. There were  
370 generally higher wind speeds and the highest median 3-hourly wind speeds of the year  
371 (MERRA-2) (Fig. 1c and 1d) in January (u: -7.6 m  $s^{-1}$  and v: -4.0 m  $s^{-1}$ ). Median winds shifted  
372 toward a more easterly source from March to May (transition time before the Habagat monsoon)  
373 (Fig. 2c to 2e) accompanied by decreasing median 3-hourly wind speeds (u = -6.8 m  $s^{-1}$ , v = -1.9  
374 m  $s^{-1}$  to u: -2.6 m  $s^{-1}$ , v = 0.2 m  $s^{-1}$ ).



375  
 376 **Figure 2:** Density plots of HYSPLIT trajectories reaching Manila Observatory per month from  
 377 2009 to 2018. Red denotes areas with the greatest number of back trajectories within a 100 km  
 378 radius. The colors represent density value contributions to Matlab-calculated cumulative  
 379 probability distribution surfaces (100 km radius) from coordinates of three-day back trajectories  
 380 of the specific months.

381 The transition times between the monsoons (when the wind directions shift and wind speeds  
 382 change) are also the times of the highest (May, Fig. 1g, 621.2 m) and lowest (November, Fig. 1g,  
 383 279.6 m) median planetary boundary layer heights (MERRA-2). The median planetary boundary  
 384 layer height was highest during the period (May) of highest temperatures, lowest relative  
 385 humidity, reduced air pressure, and lowest monthly median low cloud fraction (MERRA-2) (Fig.  
 386 1e) (1.4 %). The lowest monthly median planetary boundary layer height was observed during

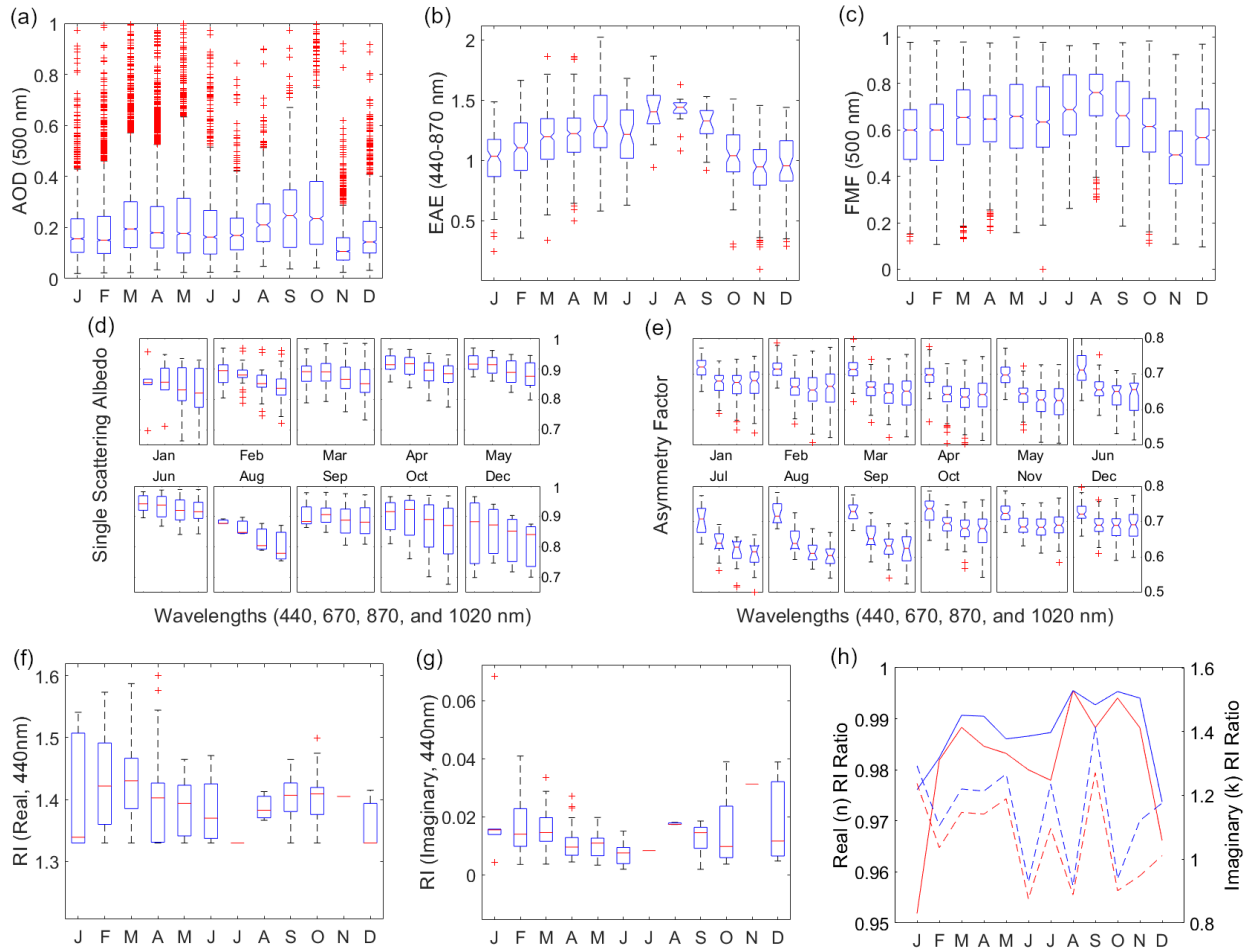
387 the period (November) when temperatures were beginning to cool and air pressure was rising.  
388 The monthly maximum low cloud fraction was lowest in July (18.5 %) during the summer  
389 southwest monsoon while the monthly median and monthly maximum low cloud fractions  
390 (MERRA-2) (Fig. 1e) were highest (38.3 % max, 4.9 % median) in January during the winter  
391 northeast monsoon.  
392

### 393 **3.2 Aerosol Particle Characteristics**

#### 394 3.2.1 Aerosol Optical Depth

395 Monthly median AOD (AERONET, 500 nm) (Fig. 3a) over the Manila Observatory was highest  
396 from August (0.21) to October (0.23) around the time of the summer monsoon when winds were  
397 coming from the southwest (Figs. 2h to 2i) (Holben et al., 2001). This is the same time of year  
398 when biomass burning activities occur in the Indonesian region southwest of Metro Manila  
399 (Glover and Jessup, 1998; Kiely et al., 2019; Cahyono et al., 2022). Studies have shown that  
400 AOD in the Philippines increases during the biomass burning season in Indonesia (Nguyen et al.,  
401 2019b; Caido et al., 2022). Regional AOD (550 nm) over the larger Southeast Asia domain from  
402 MISR and MERRA-2 (Fig. 4) had a similarly large peak around the same time beginning in  
403 September until October which, however, was second only in magnitude to a March peak, which  
404 is influenced by biomass burning in Peninsular Southeast Asia (PSEA) (Gautam et al., 2013;  
405 Hyer et al., 2013; Dong and Fu, 2015; Wang et al., 2015; Yang et al., 2022). This is consistent  
406 with the peak in speciated AOD due to fine (radii  $<0.7 \mu\text{m}$ ), spherical, and absorbing aerosols  
407 that were observed by MISR from March to April (Fig. S1). This larger peak in March,  
408 attributed to PSEA (which is  $\sim 2000$  km west of the Philippines), was not as prevalent in the  
409 AERONET AOD data over Manila Observatory in Metro Manila due to the dominant easterly  
410 winds in the Philippines in March (Fig. 2c) and more localized sources.

411

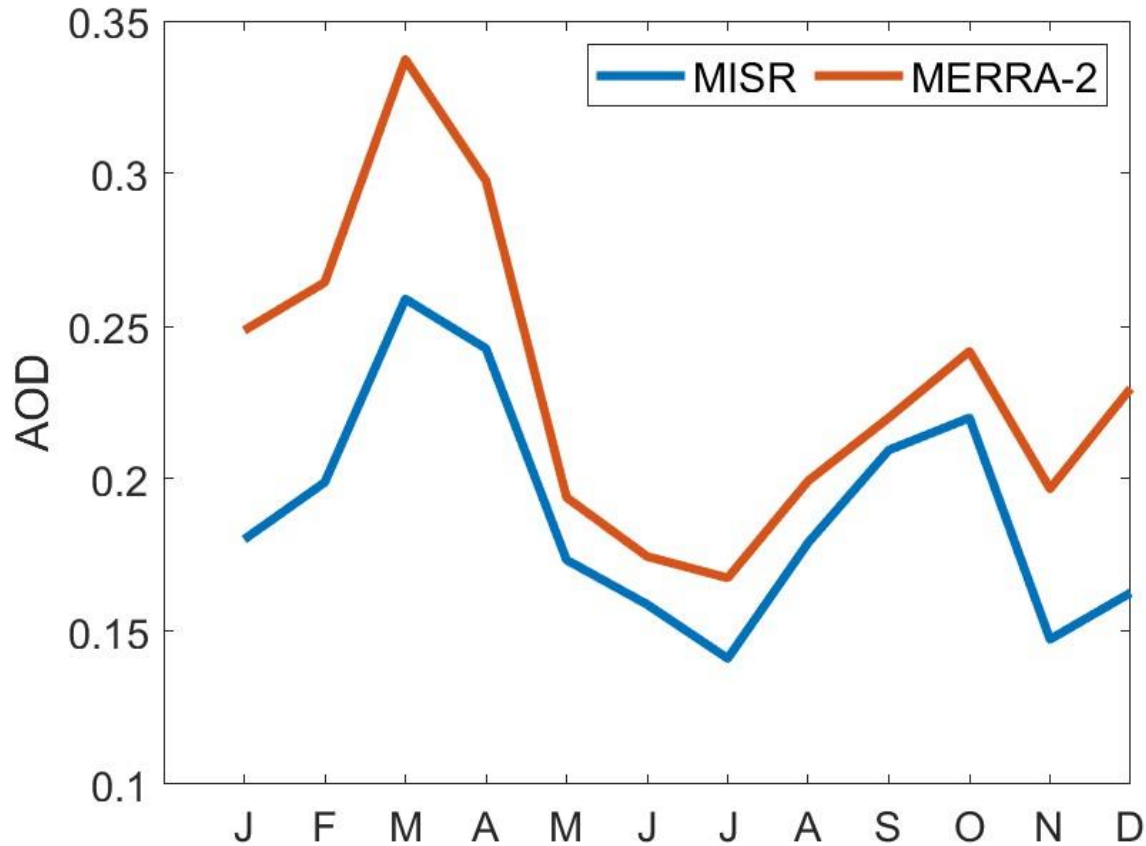


412 **Figure 3:** Monthly characteristics of AERONET aerosol particle parameters: (a) aerosol optical  
 413 depth (AOD at 500 nm with y-axis until 1.0 only for larger boxplot resolution) with counts (Jan:  
 414 2107, Feb: 3931, Mar: 4923, Apr: 5755, May: 3389, Jun: 1653, Jul: 637, Aug: 483, Sep: 718,  
 415 Oct: 1555, Nov: 2001, Dec: 1386), (b) extinction angstrom exponent (EAE at 440-870 nm) with  
 416 counts (Jan: 102, Feb: 248, Mar: 312, Apr: 309, May: 137, Jun: 53, Jul: 14, Aug: 18, Sep: 18,  
 417 Oct: 79, Nov: 77, Dec: 52), (c) spectral de-convolution algorithm (SDA) retrievals of fine mode  
 418 fraction (FMF at 500 nm) with the same counts as AOD, (d) single scattering albedo (SSA) from  
 419 440 nm (leftmost boxplot) to 1020 nm (rightmost boxplot) with counts (Jan: 6, Feb: 31, Mar: 62,  
 420 Apr: 50, May: 29, Jun: 8, Aug: 3, Sep: 5, Oct: 17, Dec: 3), (e) asymmetry factor (AF) from 440  
 421 nm (leftmost boxplot) to 1020 nm (rightmost boxplot) with the same counts as EAE, (f) real and  
 422 (g) imaginary refractive index (RI) values (440 nm) with the same counts as SSA, and (h)  
 423 refractive index ratios (where the blue line is the ratio of RI at 440 nm and 670 nm, the red line is  
 424 the ratio of RI at 440 nm and the average RI for the 675–1020 nm wavelengths, and the broken  
 425 lines are the imaginary refractive index ratios) for Metro Manila, Philippines based on data  
 426 between January 2009 and October 2018.  
 427

428 There is a notable dip in the monthly median AERONET AOD over Manila Observatory from  
 429 the peak in October to the lowest monthly median AOD (0.11) in November (Fig. 3a), just  
 430 slightly above defined background levels ( $<0.1$ ) (Holben et al., 2001), when the windspeeds  
 431 were picking up and were coming from the east to northeast directions (Fig. 2k) in the direction  
 432 of the Philippine Sea and the West Pacific Ocean. This dip was also observed in the regional

433 (30° × 30°) AOD data (MISR and MERRA-2, Fig. 4). This is most probably due to the decrease  
 434 in the AOD contribution from fine (radii <0.7 μm) and spherical particles based on size speciated  
 435 MISR AOD (Fig. S1). Larger and non-spherical particle contributions to AOD increase in  
 436 November in the Southeast Asia region. The MERRA-2 AOD is relatively higher than the MISR  
 437 AOD probably due to assimilation of MODIS data into MERRA-2. Studies in Asia (Xiao et al.,  
 438 2009; Qi et al., 2013; Choi et al., 2019) have observed relatively higher MODIS AOD compared  
 439 to MISR AOD.

440



441

442 **Figure 4:** Monthly mean AOD (550 nm) in Southeast Asia (30° × 30°) from 2009 to 2018 from  
 443 MISR (blue line) and MERRA-2 (red line).

444 There were 338 instances (~1.2 % of the time based on the total number of 28,538 valid  
 445 AERONET AOD data points) of AOD values exceeding 1, indicative of heavy aerosol particle  
 446 loading (Huang et al., 2021). Because AOD is extrinsic (it depends on mass), AOD describes  
 447 total aerosol particle loading and we examine other aerosol particle parameters from AERONET  
 448 to make more informed inferences about size and composition.

449 3.2.2 Extinction Angstrom Exponent and Fine Mode Fraction



450 The extinction angstrom exponent (EAE) relates the extinction of light at specific wavelengths  
451 and is indicative of aerosol particle size (Ångström, 1929). The EAE is usually greater for  
452 smaller particles (~4 for very small particles that undergo Rayleigh scattering, > 2 for small  
453 particles, < 1 for large particles like sea salt and dust, and 0 for particles as large as cloud drops)  
454 (Schuster et al., 2006; Bergstrom et al., 2007). The highest monthly median EAE (Fig. 3b) from  
455 2009 to 2018 over the Manila Observatory was observed from July (~1.4) to September (~1.3),  
456 during the southwest monsoon. This period is associated with the biomass burning southwest of  
457 the Philippines (Oanh et al., 2018; Stahl et al., 2021; Crosbie et al., 2022). The median (per  
458 month) EAE ranged from ~0.9 in November to ~1.4 in August, a range which is within the  
459 values from previous studies collected from mixed sites and urban/industrial areas with both fine  
460 and coarse particles (Eck et al., 2005; Giles et al., 2012). The high EAE over Manila Observatory  
461 from July to September is consistent with the regional (30° latitude x 30° longitude) MISR data  
462 that shows increased AOD from fine, spherical, and absorptive particles (Fig. S1) in Southeast  
463 Asia during the same months. This suggests that the high EAE observed at the Manila  
464 Observatory during these months is not necessarily from local sources.

465 EAE increases with AOD (Fig. S2), which means that the greater particle loading is contributed  
466 by smaller particles (Smirnov et al., 2002). Of the high loading cases (AOD >1) over Manila  
467 Observatory, the EAE values were mostly greater than 0.8 indicating fine mode particles (Che et  
468 al., 2015). The EAE values in August were the highest compared to other months including  
469 having the highest minimum value of any month (0.71) (Fig. S2), due to smaller particles (~EAE  
470 >1 for fine particles, Table 2). The lowest EAE values (0.08) and thus the largest particles were  
471 observed in December, which again may be regional in nature with MISR EAE also lowest  
472 during this time with increased AOD from larger and non-spherical particles (Fig. S1).

473 The fine mode fraction (FMF) describes the prevalence of fine mode particles in the column of  
474 air above the surface. The fine mode fraction (Fig. 3c) from 2009 to 2018 was highest in August  
475 (monthly median of 0.75) and lowest in November (monthly median of 0.45). This is consistent  
476 with the EAE values discussed earlier with the prevalence of smaller particles in August and  
477 larger particles in November. In August (Fig. 2h) the southwest monsoon is known to coincide  
478 with the transporting of fine smoke particles to Luzon. In November (Fig. 2k), the prevalent  
479 winds may have already shifted to easterly (Matsumoto et al., 2020) implying more marine-  
480 related sources associated with coarser particles.

### 481 3.2.3 Single Scattering Albedo

482 The single scattering albedo (SSA) is the most important aerosol particle parameter determining  
483 whether aerosol particles will have a warming or cooling effect (Reid et al., 1998). SSA is the  
484 ratio of the scattering coefficient to the total extinction (scattering and absorption) coefficient  
485 (Bohren and Clothiaux, 2006) of aerosol particles. Higher SSAs are related to more reflective  
486 aerosol particles while more absorbing aerosol particles will have lower SSA values; values  
487 range from 1 (reflective) to 0 (absorbing). Monthly median SSA values were largest in June  
488 (0.94 at 440 nm), suggesting the presence of more reflective aerosol particles, and smallest in  
489 August (0.88 at 440 nm and 0.78 at 1020 nm) suggesting more absorptive particles that are  
490 similar in range to the SSA of biomass burning particles (Table 2). August is when biomass  
491 burning is prevalent to the southwest of the Philippines and associated with soot particles that are  
492 absorptive.

493 The sensitivity of SSA to different wavelengths depends on the type of aerosol particles present.  
494 More specifically, aerosol particle size and refractive index (which is related to aerosol particle  
495 composition) both affect the SSA (Dubovik and King, 2000; Bergstrom et al., 2007; Moosmüller  
496 and Sorensen, 2018). For dust-type particles, SSA increases with wavelength because of lower  
497 dust absorption in the higher visible to infrared wavelengths (Dubovik et al., 2002), while for  
498 urban particles (including black carbon), which absorb light at longer wavelengths, SSA  
499 decreases with wavelength (Reid et al., 1998; Bergstrom et al., 2002). The presence of organic  
500 carbon may affect this spectral dependence; however, because organic particles absorb in the  
501 UV, this lowers SSA at wavelengths shorter than 440 nm (Kirchstetter et al., 2004). Monthly  
502 median SSA generally decreased with increasing wavelength for all months with available data  
503 (Fig. 3d) presumably due to the influence of more urban particles in contrast to dust.  
504 Noteworthy though are the monsoon transition months of April, September, and October (Fig.  
505 3d), which had increased SSA from 440 nm to 670 nm, possibly from organics along with black  
506 carbon due to transported smoke. The back-trajectories for these months (Figs. 2d, 2i, and 2j)  
507 suggest sources from the northeast that are closer to Luzon during these months compared to  
508 other months. This indicates the possibility of more local sources. Increasing the certainty of  
509 sources associated with aerosol particles necessitates looking at other available aerosol particle  
510 parameters, discussed subsequently.

#### 511 3.2.4 Asymmetry Factor

512 The asymmetry factor quantifies the direction of scattering of light due to aerosol particles, with  
513 values ranging from -1 (back scatter) to 0 (uniform scattering) to 1 (forward scatter). It is  
514 important in modeling climate forcing because it affects the vertical distribution of the radiation  
515 in the atmosphere (Kudo et al., 2016; Zhao et al., 2018). The asymmetry factor is dependent on  
516 particle size, shape, and composition and the value of 0.7 is used in radiative models (Pandolfi et  
517 al., 2018).

518 Lower asymmetry factors are related to smaller particles (at constant AOD) (Bi et al., 2014).  
519 Measured values due to biomass burning, for example, are 0.54 (550 nm) in Brazil (Ross et al.,  
520 1998) and 0.45 – 0.53 (550 nm and including dust) over central India (Jose et al., 2016). There  
521 have been relatively higher values observed in western, central, and eastern Europe (0.57 – 0.61  
522 at 520 – 550 nm) (Pandolfi et al., 2018) and the U.S. East Coast (0.7 at 550 nm) (Hartley and  
523 Hobbs, 2001). In Norway, the asymmetry factor for background summer conditions was 0.62  
524 and was higher in the springtime at 0.81 (862 nm) during Arctic haze events (Herber et al.,  
525 2002). Highest values are associated with dust such as those measured in the Sahara being 0.72 –  
526 0.73 (500 nm) (Formenti et al., 2000). Over Metro Manila, the asymmetry factors from the  
527 AERONET data at the 675, 870, and 1020 nm were similar across months (Fig. 3e). The monthly  
528 median asymmetry factors at 440 nm ranged from 0.70 (April and May) to 0.74 (October), while  
529 for 670, 870, and 1020 nm the monthly median asymmetry factors were smaller and ranged from  
530 0.62 – 0.69. These values were closely related to those observed over the U.S. East Coast as  
531 mentioned earlier, perhaps due to the proximity of the location to the coast (10 km east of Manila  
532 Bay and 100 km west of the Philippine Sea) as well as its location in Manila, which is a large  
533 local source due mostly to vehicles (Cruz et al., 2019).

534 The monthly median asymmetry factor in Metro Manila was greatest towards the end of the year  
535 (October to December) for all the wavelengths, suggesting larger particles when winds (Figs. 2j  
536 to 2l) come from the Philippine Sea in the northeast. It was in March and April that the monthly

537 median asymmetry factor was minimal for 440 nm and in August for 670, 870, and 1020 nm.  
538 These were the times when aerosol particles were smallest. March to April represents the driest  
539 time of the year in Manila (Fig. 1b and 1h) perhaps preventing particle growth and where the  
540 local sources may be dominating, even as back-trajectories (Fig. 2c and 2d) extend all the way  
541 from the Philippine Sea to the east. This is corroborated by results from other studies showing  
542 that the asymmetry factor seems to be enhanced by relative humidity (Zhao et al., 2018). The  
543 unexpected low asymmetry factor values in August, however, are probably because of the source  
544 of the particles. August had the highest relative humidity and precipitable water (Fig. 1b and 1h)  
545 but is also when the back-trajectories (Fig. 2h) were from the southwest, possibly affected by the  
546 Indonesia fires, which could have transported more non-hygroscopic fine particles.

547 Fine particles have been observed to exhibit decreasing asymmetry factors with increasing  
548 wavelength (Bergstrom et al., 2003). This trend is observed in all the months for the monthly  
549 median asymmetry factors (Fig. 3e) suggesting the predominance of smaller aerosol particles.  
550 The greatest decrease in the asymmetry factor (all wavelengths) was in August, consistent with  
551 the lowest observed values of the year (670, 870, and 1020 nm). Transported biomass burning  
552 particles are the probable dominant particles during this time. They are usually composed of  
553 hygroscopic inorganics, non-hygroscopic soot, and relative non-hygroscopic organic fractions  
554 (Petters et al., 2009). Knowing the composition of biomass burning particles over the study  
555 region will help in the understanding of hygroscopicity and its impacts on radiation.

### 556 3.2.5 Refractive Index

557 Refractive index is an intrinsic parameter as it does not depend on the mass or the size of  
558 particles, and thus can be used to infer aerosol particle composition (Schuster et al., 2016). For  
559 the case of the AERONET data, which include refractive index values that are insensitive to  
560 coarse particles (Sinyuk et al., 2020), the focus of the discussion will be for fine mode particles  
561 and may be limited when coarse particles are involved. Refractive index measurements are  
562 complex since they include real and imaginary parts related to light scattering and absorption,  
563 respectively. All aerosol particles scatter light but only certain types absorb light significantly.  
564 The most prominent particle absorbers in the atmosphere are soot carbon, brown carbon (organic  
565 carbon that absorbs light), and free iron from dust (hematite and goethite in the ultraviolet to  
566 mid-visible) (Schuster et al., 2016). For this study, we examine refractive index values at 440 nm  
567 wavelength. Pure sources of soot carbon have the highest real refractive index values (~1.85) as  
568 well as the highest imaginary refractive index (~0.71), both independent of wavelength (Koven  
569 and Fung, 2006; Van Beelen et al., 2014). Brown carbon and dust have relatively lower real  
570 refractive index values at 440 nm (~1.57 and ~1.54) and imaginary refractive index values  
571 (~0.063 and ~0.008) that decrease with increasing wavelength (Xie et al., 2017).

572 In this study the range of the monthly median real refractive index values (440 nm) was from  
573 1.33 (December and January) to 1.43 (March) (Fig. 3f). Water uptake by aerosol particles  
574 decreases the real refractive index values (Xie et al., 2017) and thus the lowered real refractive  
575 indices over the Manila Observatory can be due to the presence of more water in the atmosphere  
576 in general and/or the increased presence of more hygroscopic particles. December and January  
577 are not necessarily the months that have the highest moisture content, but they are months when  
578 back-trajectories reaching the column over the Manila Observatory are from the Philippine Sea  
579 to the northeast presumably transporting hygroscopic particles. As reported in previous sections,  
580 relatively larger particles are observed around this time of the year and thus sea salt can be an

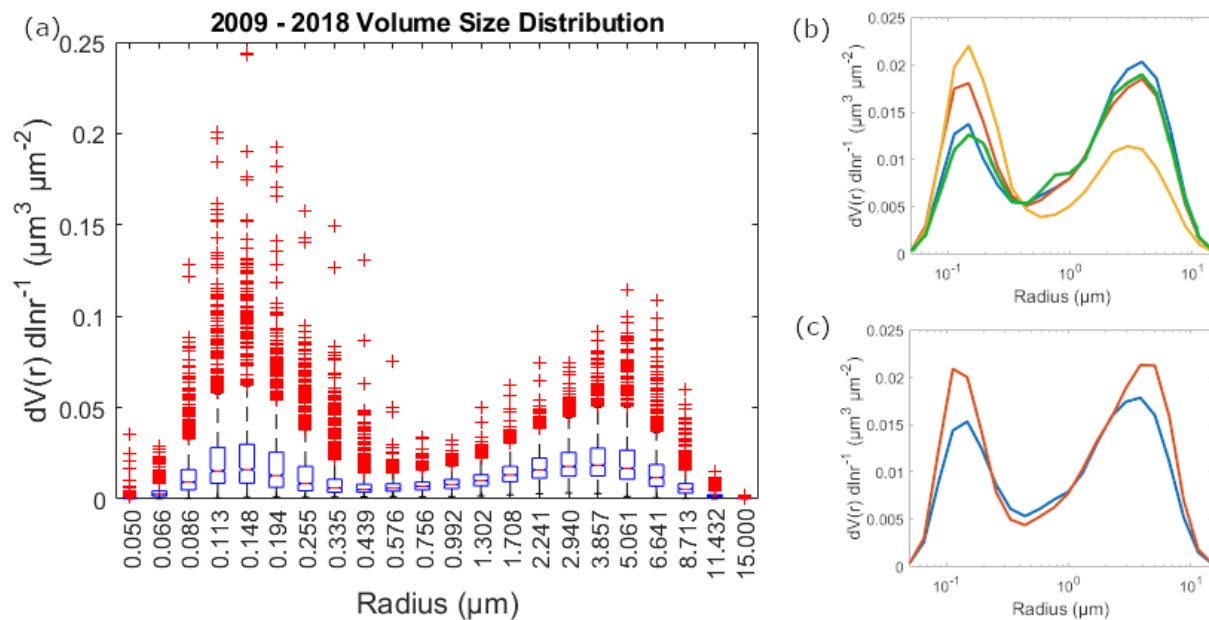
581 important contributor. The greatest change in the monthly median real refractive index with  
582 increasing wavelength also was observed in December (Fig. 3h), possibly due the increased  
583 fractional contribution of constituents other than soot carbon (because the real refractive index of  
584 soot carbon is invariant with wavelength). Noteworthy as well is the month of August (Fig. 3f),  
585 which has the smallest range of real refractive index values, possibly indicating a more  
586 homogenous aerosol particle source compared to other months. August is the month with the  
587 highest relative humidity (Fig. 1b) as well as highest precipitable water (Fig. 1h), while this is  
588 also the month when long-range biomass burning emissions are observed to be highest, and  
589 when the real refractive index values would otherwise be expected to be highest.

590 Water content seems to play a significant role in the real refractive index values in Manila.  
591 March, when the monthly median real refractive index values are highest (Fig. 3f), is when  
592 precipitable water vapor (Fig. 1h) is among the lowest in the year. The months around March are  
593 also when maximum real refractive indices (1.57 in February, 1.59 in March, and 1.60 in April)  
594 were observed (Fig. 3f). March was when there was a relatively small change in real refractive  
595 index value with wavelength perhaps related to greater soot carbon fractions during this time,  
596 due possibly to the contribution of biomass burning from Peninsular Southeast Asia (Shen et al.,  
597 2014). Looking more closely at the imaginary refractive index values will help elucidate this  
598 issue.

599 Monthly median imaginary refractive index values (440 nm) ranged from 0.007 in June to 0.015  
600 in September and December (Fig. 3g). These are low compared to those of the pure soot carbon  
601 mentioned earlier because of the mixed nature of the sampling site with contributions from  
602 brown carbon and dust. The highest imaginary refractive index values in September and  
603 December suggest the greatest fractional contribution of soot because the highest imaginary  
604 refractive index values are associated with soot. These are also similar in magnitude to biomass  
605 burning particles in the Amazon (0.013) (Guyon et al., 2003). The key distinction between soot  
606 carbon and other major absorbers (brown carbon and dust) is that its imaginary refractive index  
607 is invariant with wavelength. Both brown carbon and dust exhibit a decrease in the imaginary  
608 refractive index with increasing wavelength (Xie et al., 2017). The ratios of imaginary refractive  
609 index values (440 nm to average of 670–1020 nm) (Fig. 3h) show a relative invariance with  
610 wavelength (ranging from 0.88 to 1.4), which indicates the dominance of soot as the major  
611 absorber in the region (Eck et al., 2003). While observed wavelength invariance points to high  
612 soot contributions, the size of the particles can help distinguish between brown carbon, which  
613 reside mainly in the fine mode, and dust sources, which yield more coarse particles (Schuster et  
614 al., 2016). September is during the southwest monsoon, which is when, as noted in the earlier  
615 sections, fine particles were most prevalent. This is also the time when the imaginary refractive  
616 index varied most with wavelength (1.4 ratio of the imaginary refractive index at 440 nm and the  
617 imaginary refractive index average for 670 nm to 1020 nm in Fig. 3h) possibly with greater  
618 absolute contributions from brown carbon, even with the highest soot carbon fractional  
619 contributions. Brown carbon has been observed both from primary and aged aerosol particle  
620 emissions from biomass burning (Saleh et al., 2013). As noted earlier, December also had the  
621 highest imaginary refractive index values as well as relatively coarser particles, possibly due to  
622 larger dust absolute contributions even with the highest soot carbon fraction contributions. The  
623 lowest monthly median imaginary refractive index values in June, on the other hand, when fine  
624 mode particles prevail suggest highest fractional contributions of brown carbon relative to other  
625 months (Fig. 3h).

626 3.2.6 Volume Size Distributions

627 The volume size distribution (VSD) is another way to be able to more deeply characterize  
 628 aerosol particles, specifically related to their effect on climate, weather, and clouds (Haywood  
 629 and Boucher, 2000; Feingold, 2003). In the Manila Observatory dataset, there was a bi-modal  
 630 VSD for the entire dataset (Fig. 5a). The fine mode median values peaked in the accumulation  
 631 mode at 0.148  $\mu\text{m}$  particle radius while the coarse mode median values peaked at 3.857  $\mu\text{m}$  (Fig.  
 632 5a and Table S1). The median coarse mode amplitudes and volume concentrations were higher  
 633 than the fine mode amplitudes and volume concentrations for most of the year (DJF, MAM, and  
 634 SON, Fig. 5b and Table S1), except during the southwest monsoon (JJA) when the fine mode  
 635 amplitude and volume concentration was higher. This is consistent with observations earlier of  
 636 fine mode prevalence during the southwest monsoon. Median VSD amplitudes (Fig. 5c) were  
 637 greater in the afternoon, with higher peaks and volume concentrations for both the fine and  
 638 coarse modes, compared to the morning. There was a slightly larger coarse median amplitude  
 639 and volume concentration, compared to the accumulation mode median amplitude and volume  
 640 concentration, for both the morning and afternoon size distributions. While the VSDs confirm  
 641 several observations based on the analysis of the aerosol particle parameters presented earlier,  
 642 not much further information is gained especially regarding chemical composition. Size  
 643 distributions are a result of contributions from multiple sources, and thus being able to  
 644 discriminate the sources based on their characteristic size distributions will help identify relevant  
 645 sources.  
 646



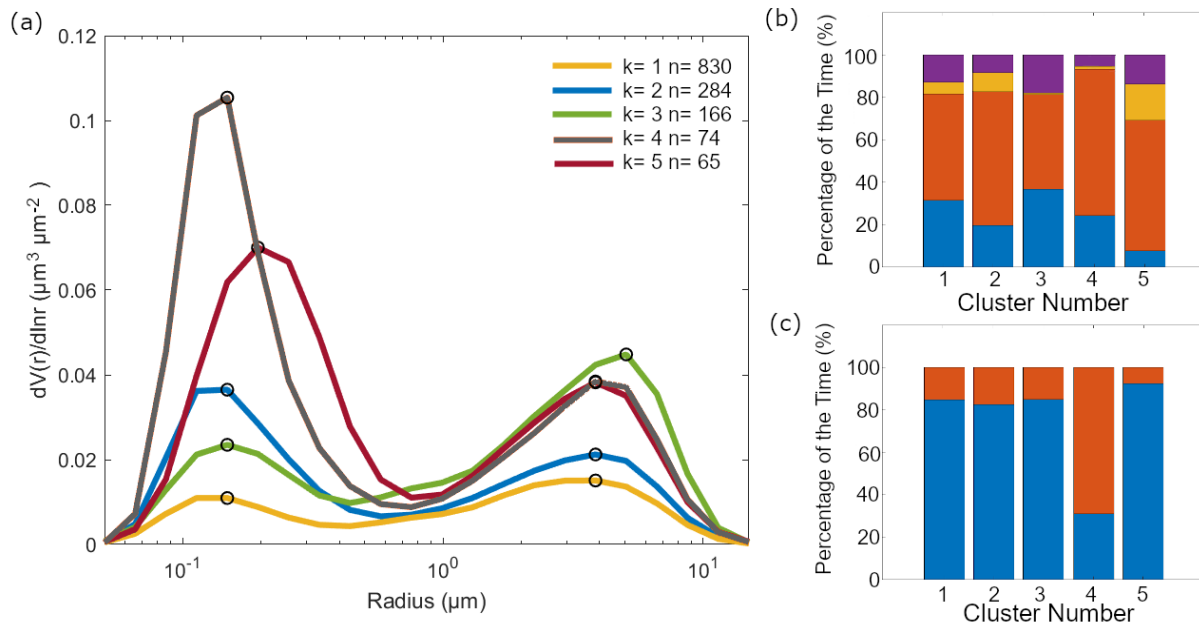
647  
 648 **Figure 5:** (a) VSD results derived from AERONET measurements at Metro Manila between  
 649 January 2009 and October 2018. Median VSDs over the study period based on (b) season (blue:  
 650 DJF, red: MAM, orange: JJA, green: SON) and (c) time of day (blue: AM, red: PM).

651  
 652 **3.3 Clusters**

653 3.3.1 VSD Cluster Profiles

654 Five clusters were identified to best represent the VSD (Fig. 6a). The average of the VSDs in  
 655 each cluster varied depending on the height of the peaks in the accumulation mode and the  
 656 coarse mode. In Metro Manila, the accumulation mode is associated with aged aerosol particles  
 657 and combustion (Cruz et al., 2019). The majority of the data (830 count out of 1419 total VSD  
 658 profiles) were clustered together in a profile (cluster 1) that had relatively low average  
 659 magnitudes of volume concentration for both the accumulation ( $0.01 \mu\text{m}^3 \mu\text{m}^{-2}$ ) and coarse ( $0.02$   
 660  $\mu\text{m}^3 \mu\text{m}^{-2}$ ) modes, with the volume concentration magnitude of the coarse mode peak slightly  
 661 higher than the volume concentration magnitude of the accumulation mode peak. The next  
 662 prevalent cluster profile (284 counts, cluster 2) had an average fine mode peak for the volume  
 663 concentration ( $0.04 \mu\text{m}^3 \mu\text{m}^{-2}$ ) which was more than twice as much than the previous profile but  
 664 with a similar coarse mode peak for the volume concentration ( $0.02 \mu\text{m}^3 \mu\text{m}^{-2}$ ). The average  
 665 coarse mode peak for the volume concentration ( $0.04 \mu\text{m}^3 \mu\text{m}^{-2}$ ) was the highest (compared to  
 666 the four other cluster profiles) for the third prevalent cluster profile (166 counts, cluster 3);  
 667 cluster 3 also had a slightly shifted volume concentration peak in the coarse mode to a higher  
 668 radius ( $5.06 \mu\text{m}$ ) compared to other clusters. The coarse mode dominated this VSD compared to  
 669 other profiles (lower magnitude for the accumulation mode peak for the volume concentration,  
 670  $0.02 \mu\text{m}^3 \mu\text{m}^{-2}$ ). The two remaining cluster profiles exhibited high average magnitudes of  
 671 volume concentration in both the accumulation and coarse modes. The fourth prevalent cluster  
 672 profile (74 counts, cluster 4) had the highest average absolute magnitude for the volume  
 673 concentration in the accumulation mode ( $0.11 \mu\text{m}^3 \mu\text{m}^{-2}$ ), while the fifth prevalent cluster profile  
 674 (65 counts, cluster 5) had a slightly smaller accumulation mode peak for the volume  
 675 concentration ( $0.07 \mu\text{m}^3 \mu\text{m}^{-2}$ ) that was shifted to a slightly higher radius ( $0.19 \mu\text{m}$  compared to  
 676  $0.15 \mu\text{m}$ ). Both clusters 4 and 5 had similar average coarse mode peak volume concentration  
 677 magnitudes ( $0.04 \mu\text{m}^3 \mu\text{m}^{-2}$ ).

678



679

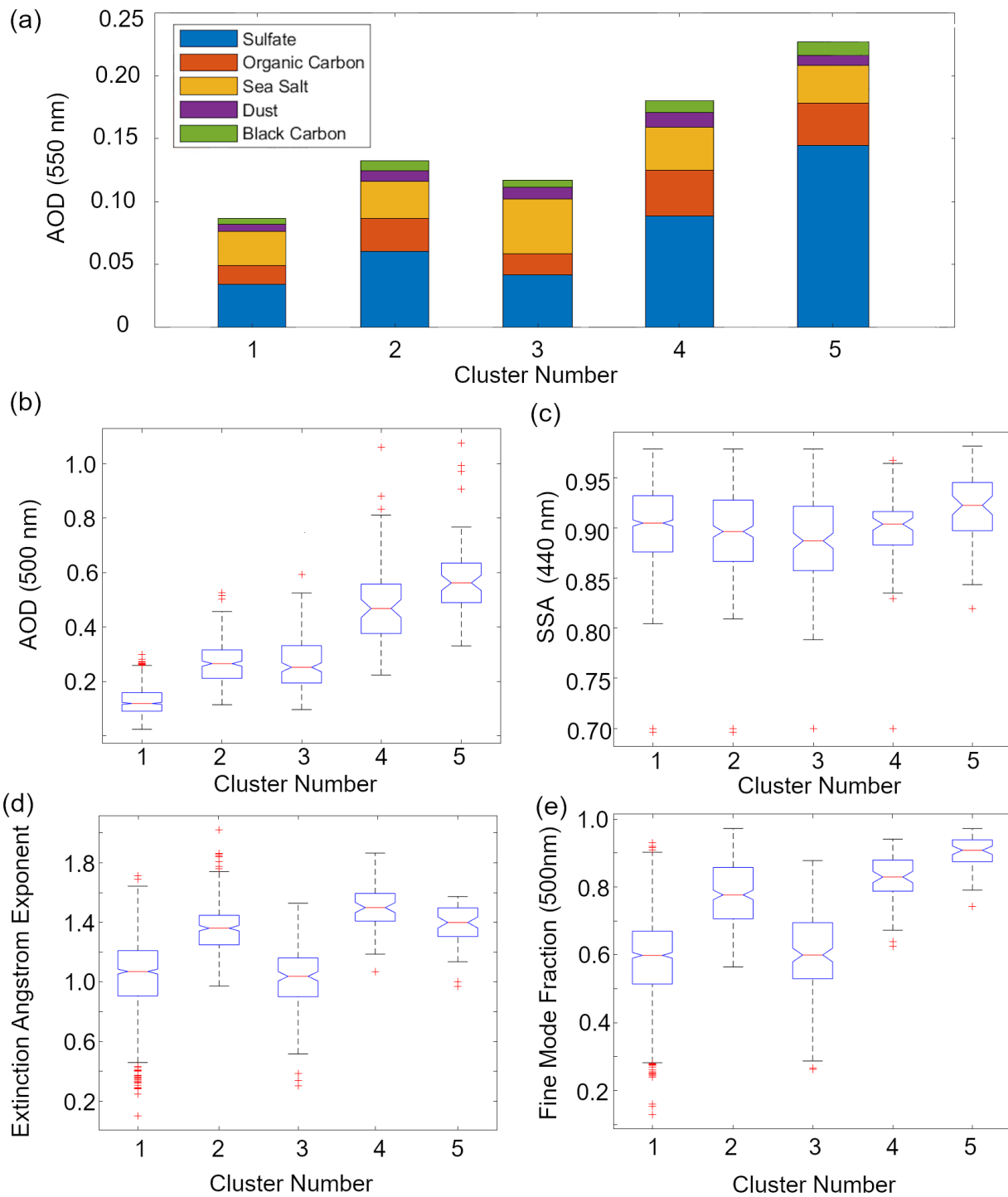
680 **Figure 6:** (a) Cluster analysis of VSD data yielding five characteristic and averaged VSDs with  
 681 the number of points per cluster shown in the legend. The black circles on the curves show the

682 peak locations in the submicrometer ( $<1 \mu\text{m}$ ) and coarse ( $\geq 1 \mu\text{m}$ ) modes. The relative abundance  
683 of each cluster is shown for different (b) seasons (blue: DJF, red: MAM, orange: JJA, violet:  
684 SON) and (c) times of day (blue: AM, red: PM).

685 The clusters were distributed across seasons (Fig. 6b), with clusters 1 and 2 being the most  
686 evenly distributed among the clusters. Cluster 3, which had the highest coarse mode peak, had  
687 the greatest contribution from September to November compared to other clusters. Cluster 4,  
688 which had the highest accumulated mode peak compared to other clusters, had the greatest  
689 contribution from March to May as well as to afternoon VSDs compared to other clusters (Fig.  
690 6b and 6c). Relative contributions of VSDs from June to August were highest for cluster 5,  
691 which had the shifted accumulated mode peak.

692 Median total (AERONET) AOD values (Fig. 7b) were lowest (0.12) for cluster 1, though it had  
693 the second highest sea salt fractional contributions (31%) (Fig. 7a) to total AOD (MERRA-2)  
694 among all the clusters. Cluster 2 had relatively mid-range median total AOD values (0.27) that,  
695 along with clusters 4 and 5, were dominated by sulfate and organic carbon (46% and 20%).  
696 Cluster 3 had similar, but slightly lower median total AOD (0.25) compared to cluster 2. Cluster  
697 3 was distinct because it had the largest total (0.04) and fractional contribution (37%) from sea  
698 salt among all clusters. Clusters 4 and 5 had the highest median total AOD values (0.47 and  
699 0.56), with cluster 5 having the highest absolute and fractional sulfate contributions (0.14 and  
700 64%) among the clusters. Integrating the above results with their corresponding aerosol particle  
701 properties can help associate the clusters to air masses.

702



703  
 704 **Figure 7:** (a) Average compositional contributions to aerosol optical depth (AOD at 550 nm)  
 705 from MERRA-2 per identified cluster (counts per cluster from 1 to 5: 830, 284, 166, 74, 65).  
 706 Boxplots of AERONET (b) total AOD (500 nm), (c) single scattering albedo (SSA at 440 nm),  
 707 (d) extinction angstrom exponent (EAE at 440 nm – 870 nm total), and (e) fine mode fraction  
 708 (FMF at 500 nm) per cluster.

709  
 710 3.3.2 Air Mass Types



711 Air masses have been classified in previous studies based on their AOD, EAE, FMF, and SSA  
712 values (e.g., Lee et al., 2010 and Aldhaif et al., 2021). The criteria from different studies (Table  
713 2) were applied per cluster. Median total AOD of cluster 1 (0.12) was less than 0.2 (Fig. 7b),  
714 which is the threshold for sea salt sources. Half of the data points in cluster 1 also fall below the  
715 threshold for clean environments (AOD < 0.1) (Sorooshian et al., 2013). Based on its median  
716 EAE (1.07, where EAE < 1 is coarse and EAE > 1 is fine) and FMF (0.60) values (Fig. 7d and  
717 7e), cluster 1 is a mixture of fine and coarse particles. The fine Cluster 1 is the only cluster with a  
718 median that meets that threshold value for clean marine sources (AOD < 0.2), and we know from  
719 Sect. 3.3.1 that its average VSD magnitude was greater for the coarse fraction and that its sea salt  
720 contribution to total AOD was second greatest among the clusters. Thus, most probably, cluster 1  
721 is a background clean marine source, since it also is predominant throughout the seasons (Fig.  
722 6b). This makes sense given the proximity of the ocean to Metro Manila from both the east and  
723 the west. The median SSA (0.90 at 440 nm) for cluster 1 (Fig. 7c), however, suggests the  
724 presence of absorbing particles most probably due to high black carbon in the local source (Cruz  
725 et al., 2019) that is mixed in with this generally clean marine source.

726 Most of the data from the other clusters all fall in the polluted category (Table 2), based on their  
727 median total AODs (>0.1) (Fig. 7b). Cluster 2 has a median FMF value of 0.78 (Fig. 7e), which  
728 suggests that most of the particles in this air mass are in the fine fraction. They are, however, not  
729 sufficiently dominant in the aerosol for them to be typical of urban/industrial sources. The  
730 average VSDs (Fig. 6a) of cluster 2 similarly suggest that their relative accumulation mode  
731 magnitude is higher than the coarse magnitude, but not much higher. Like cluster 1, cluster 2 is  
732 also more evenly distributed across the seasons (Fig. 6b). The median SSA for cluster 2 (0.90 at  
733 440 nm) is also similar to the SSA of cluster 1 (Fig. 7c) where the local and background particles  
734 are mixed. Cluster 2 could be a fine polluted background source superimposed on the dominant  
735 marine source. Metro Manila is a megacity with continuous and large amounts of sources that  
736 could be, due to its proximity to the ocean, interacting with the background.

737 Based on its median EAE value (1.04) (Fig. 7d), cluster 3 is mixed but mostly in the coarse  
738 fraction, consistent with its VSD profile (Fig. 6a) which has the highest coarse magnitude (FMF  
739 = 0.60) compared to the other clusters. The contribution of data from September to February is  
740 greatest in cluster 3, consistent with expected coarser particles during this period when the winds  
741 are initially shifting from the southwest before becoming more northeasterly, as previously  
742 noted. Median SSA (0.89 at 440 nm) was lowest for cluster 3 (Fig. 7c), this and the relatively  
743 high coarse particle contribution suggests cluster 3 as a possible dust source based on past  
744 studies (Lee et al., 2010). This air mass can be a mixture of local sources and transported dust air  
745 masses, the large sea salt contribution (~37%) to total AOD (Sect. 3.3.1) can be related to long-  
746 range transport.

747 Both clusters 4 and 5 have median total FMF (0.83 and 0.91) (Fig. 7e) values exceeding the mark  
748 (> 0.8, Table 2) for urban/industrial air masses. Combining this and results from the previous  
749 sections confirms that cluster 4 can be an urban/industrial source given that it had the highest  
750 median accumulated mode peak and organic carbon contribution (~20%) to total AOD among  
751 the clusters. The median SSA for cluster 4 (0.90 at 440 nm) was similar to the median SSA of  
752 clusters 1 and 2 (Fig. 7c), but the maximum SSA value for this cluster was lowest in general  
753 among all the clusters suggesting cluster 4 has the net most absorptive effect. The cluster 4 air  
754 mass is probably from local sources and transported biomass burning emissions. The high

755 median EAE (1.40, Fig. 7d) may be associated with aerosol particles due to biomass burning  
756 (Deep et al., 2021).

757 Cluster 5 had the highest median total AOD (0.56) and FMF (0.91) values (Fig. 7b and 7e). It  
758 also had the highest sulfate contribution (~64%) to total AOD (Fig. 7a), the highest median SSA  
759 (0.92 at 440 nm, thus most reflective particles among the clusters) (Fig. 7c), and a shifted  
760 accumulation mode peak (Fig. 6a). These characteristics suggest that cluster 5 is a possible cloud  
761 processing air mass (Eck et al., 2012). The larger peak in the accumulation mode is possibly the  
762 cloud signature. Previous studies have attributed this larger mode to cloud processing due to the  
763 conversion of SO<sub>2</sub> to sulfate (Hoppel et al., 1994). Cloud processing is a major source of sulfate  
764 (Barth et al., 2000).

765 The distribution of the air masses based on the abundance of the VSD profiles per cluster suggest  
766 prevalent clean marine (58% of the total VSD counts) and background fine polluted (20%) air  
767 masses over Metro Manila. The mixed dust (12%), urban/industrial (5%), and cloud processing  
768 (5%) air masses contribute 22% altogether. We can investigate more deeply and look at specific  
769 case studies that can better describe the air masses identified here.

770

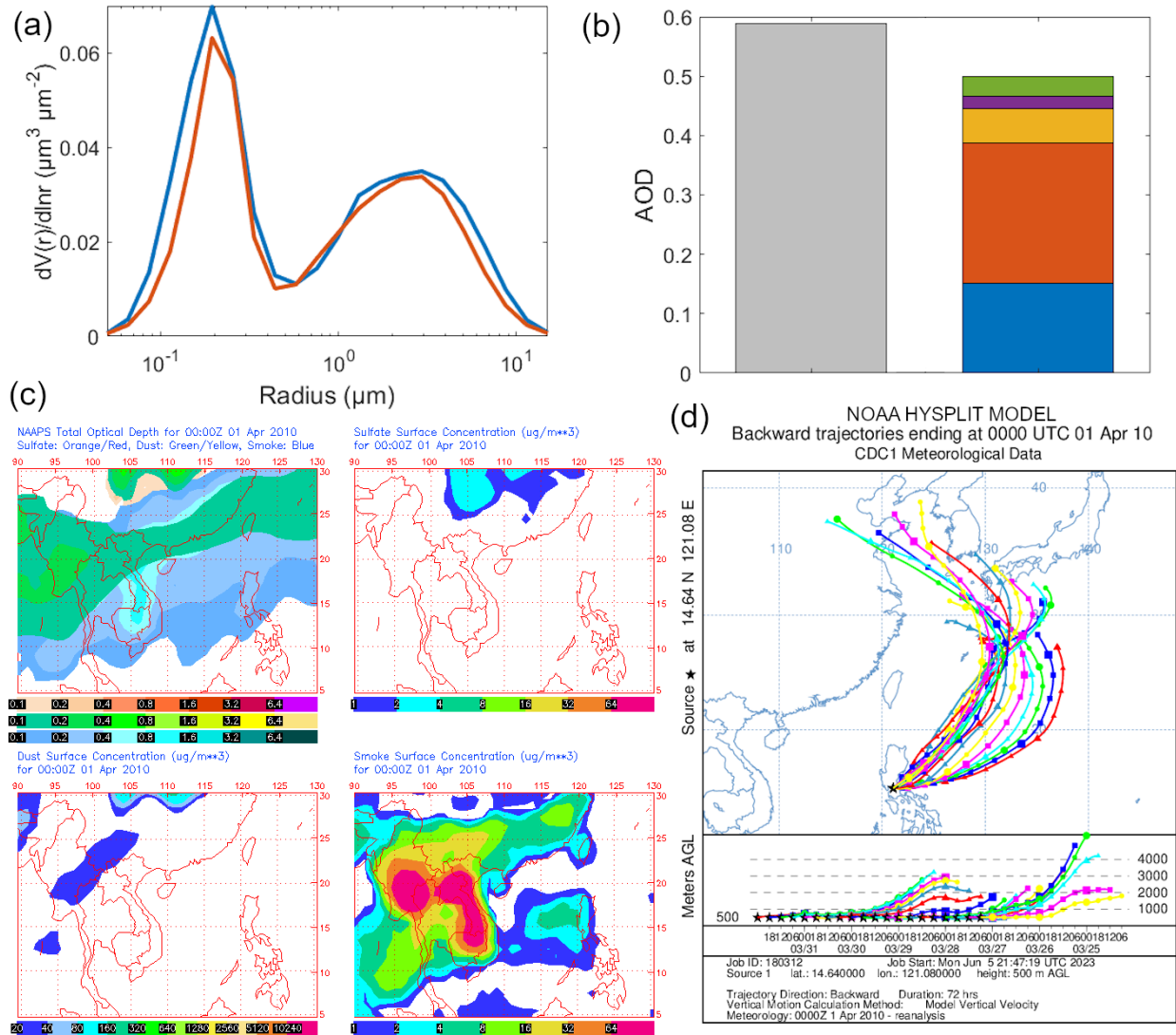
### 771 **3.4 Case Studies**

772 Selected case studies are used to highlight periods with the highest AOD values and strongest  
773 clear sky (no rain and heavy clouds) daytime aerosol particle sources within the sampling period.  
774 As such, the clusters that are associated with the selected case studies are the clusters (3-5) with  
775 higher VSD concentration magnitudes.

776

#### 777 **3.4.1 Long Range Transport of Smoke**

778 Both cases of long-range transport of smoke discussed below have similar VSDs (Fig. 8a and 9a)  
779 to the urban/industrial cluster VSD (cluster 4, Fig. 6a). Organic carbon was the dominant  
780 contributor to AOD (Fig. 8b and 9b) for both long-range transport cases. The first of two events  
781 occurred around 1 April 2020 with smoke presumed to come from East Asia. The VSD of this  
782 specific case (Fig. 8a) is most like the urban/industrial cluster (cluster 4 in 3.3.2, Fig. 6a) because  
783 of the high magnitude of its accumulated mode peak, its timing (April), and the enhanced  
784 organic carbon contribution to AOD in the area (Fig. 8b). Though the absolute black carbon  
785 contribution to AOD was highest here compared to the other case studies, and in general for the  
786 AERONET data, it was organic carbon that was more prevalent in terms of contribution to total  
787 AOD. Smoke is comprised of both soot carbon and organic carbon, amongst other constituents  
788 (Reid et al., 2005).



789

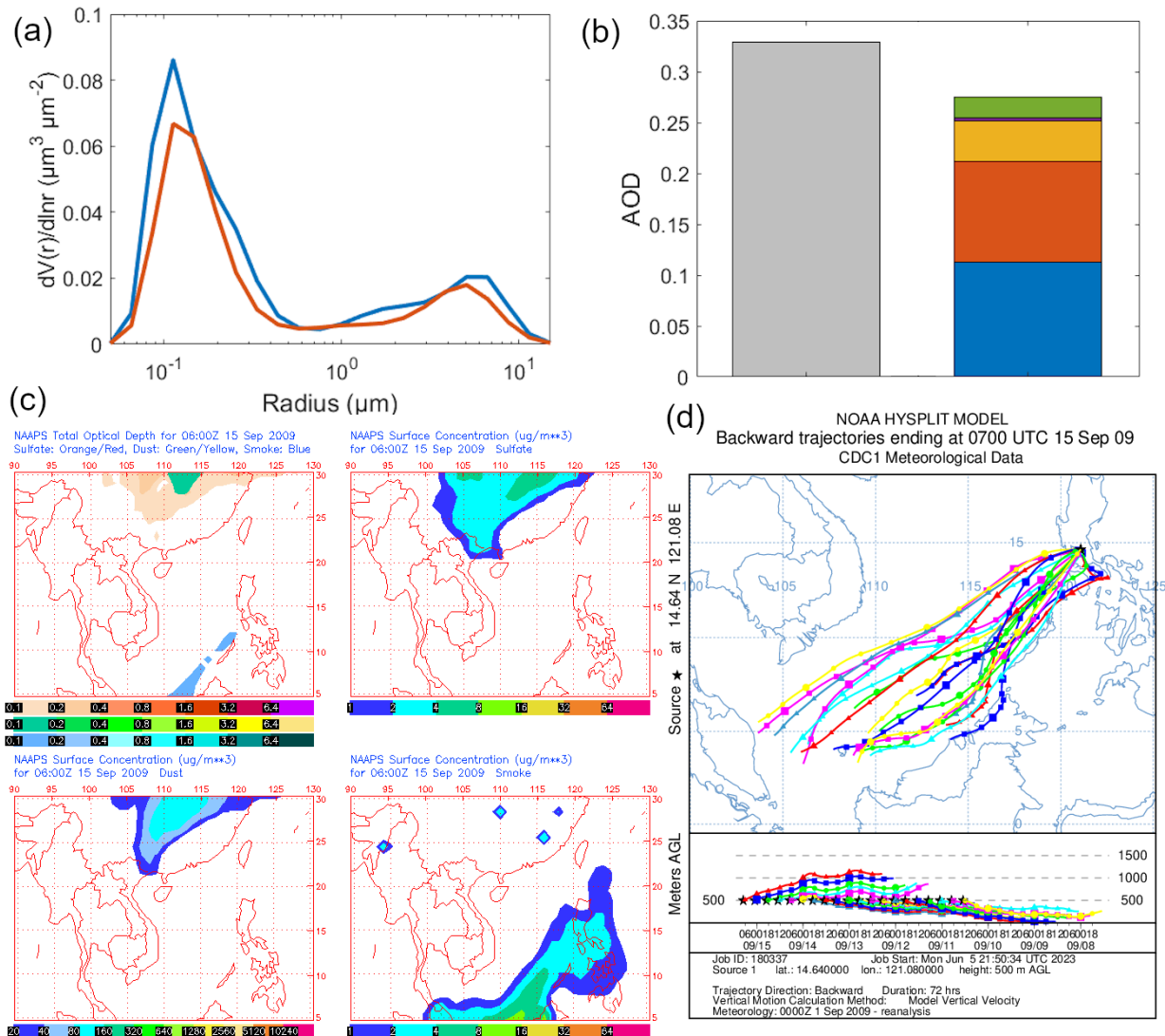
Apr 1 02:30:48 2010 NRL/Monterey Aerosol Modelling

790 **Figure 8:** Case study of long-range transport (smoke – East Asia) around 1 April 2010. (a)  
 791 AERONET VSDs at (blue) 00:01 and (red) 00:26 UTC, (b) AOD from AERONET (gray:  
 792 median AOD at 500 nm) and MERRA-2 hourly (green: black carbon, violet: dust, yellow: sea  
 793 salt, orange: organic carbon, blue: sulfate) compositional contributions to AOD (550 nm) closest  
 794 in time to 00:01 UTC, (c) NAAPS maps of total and compositional hourly AOD (orange/red:  
 795 sulfate, green/yellow: dust, blue: smoke) and sulfate, dust, and smoke surface concentrations at  
 796 00:00 UTC, and (d) HYSPLIT seven-day back-trajectories arriving at Manila Observatory at  
 797 00:00 UTC.

798 The smoke contribution to AOD from NAAPS (Fig. 8c) for the first smoke case was visible in  
 799 the Philippines (0.2) and seemed to come from East Asia were the smoke contribution to AOD  
 800 was greater (reaching 0.8) especially in Peninsular Southeast Asia. Smoke surface concentrations  
 801 were also widespread (Fig. 8c) with greatest concentrations in East Asia that reached the  
 802 Western Philippines, though seemingly disconnected over the sea. There were observed biomass  
 803 burning emissions in the Peninsular Southeast Asia (southern China, Burma, and Thailand) at

804 this time (Shen et al., 2014). The direction of the air mass coming into Metro Manila was from  
805 the northeast, which curved from the west in the direction of East Asia based on HYSPLIT back-  
806 trajectories (Fig. 8d).

807 The second smoke case was on 15 September 2009 with the source being Southeast Asia. The  
808 back-trajectories of this case study (Fig. 9d) are from the southwest of the Philippines, and in the  
809 direction of the Malaysia and Indonesia. NAAPS maps likewise show elevated AOD,  
810 specifically smoke contribution to AOD (Fig. 9c), as well as enhanced smoke surface  
811 contributions in the area around Metro Manila for this second smoke case study. The observed  
812 AOD and smoke surface concentration increased specifically from the southwest of the  
813 Philippines in the same direction of the back-trajectories. There were fires in the lowland (peat)  
814 forests of Borneo around this time (NASA, 2009). MERRA-2 AOD contributions for this case  
815 were greatest due to organic carbon as well as sulfate (Fig. 9b), and the absolute black carbon  
816 contributions were greatest compared to other cases. The VSD of this smoke case from Southeast  
817 Asia (Fig. 9a) resembled that from long-range transported smoke from East Asia (Fig. 8a) and  
818 the urban/industrial air mass (cluster 4, Fig. 6a). This case occurred in the afternoon, which was  
819 the prevalent time that the urban/industrial air mass was observed (Fig. 6c).

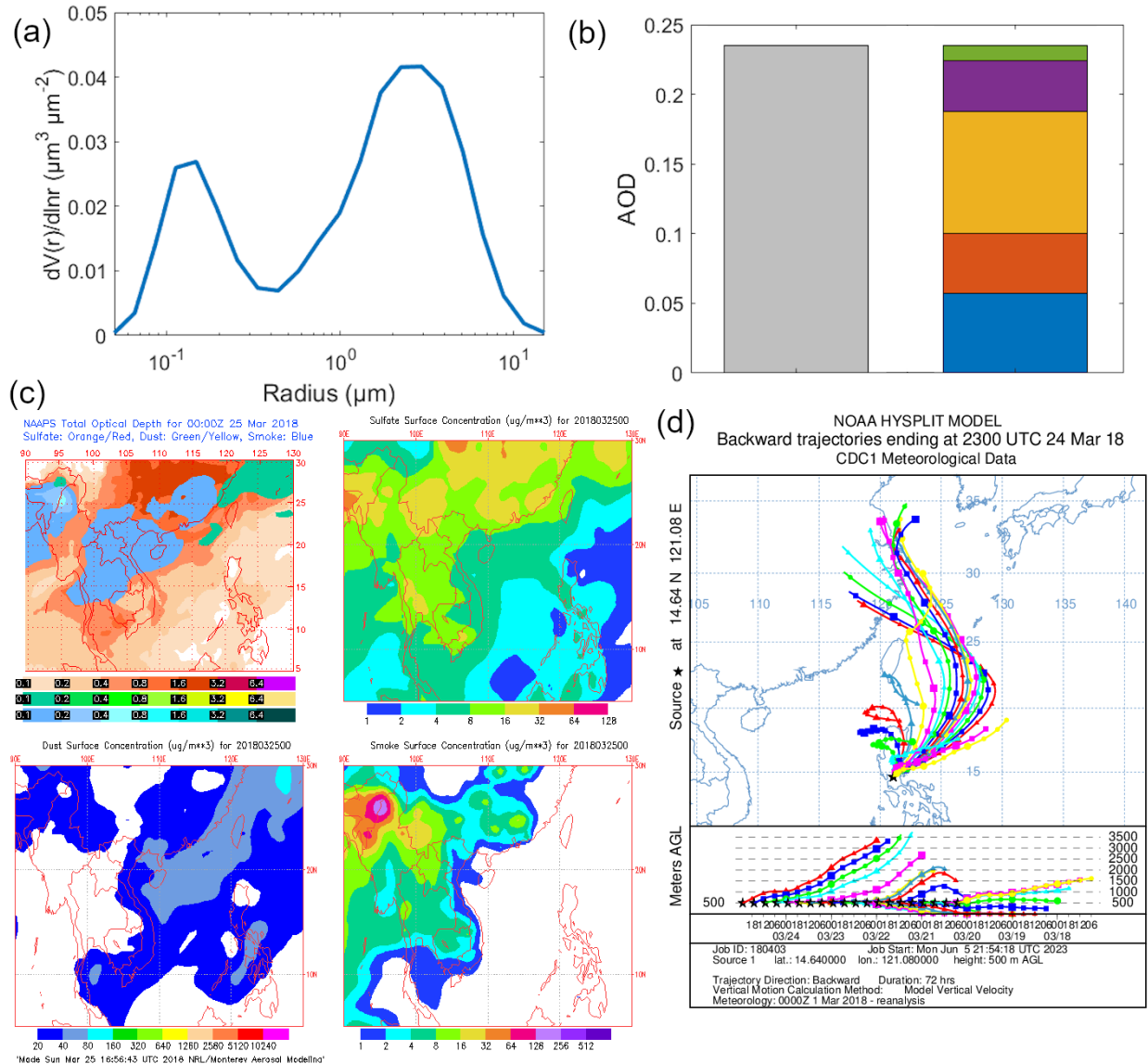


820  
 821 **Figure 9:** Case study of long-range transport (smoke – Southeast Asia) around 15 September  
 822 2009. (a) AERONET VSDs at (blue) 07:27 and (red) 07:52 UTC, (b) AOD from AERONET  
 823 (gray: median AOD at 500 nm) and MERRA-2 hourly (green: black carbon, violet: dust, yellow:  
 824 sea salt, orange: organic carbon, blue: sulfate) compositional contributions to AOD (550 nm)  
 825 closest in time to 07:27 UTC, (c) NAAPS maps of total and compositional hourly AOD  
 826 (orange/red: sulfate, green/yellow: dust, blue: smoke) and sulfate, dust, and smoke surface  
 827 concentrations at 06:00 UTC, and (d) HYSPLIT seven-day back-trajectories arriving at Manila  
 828 Observatory at 07:00 UTC.  
 829

### 830 3.4.2 Long Range Transport of Dust

831 The VSD of this specific case on 24 March 2018 (Fig. 10a) was most similar to the mixed dust  
 832 cluster (cluster 3), which had a mixed size distribution but a more dominant coarse contribution.  
 833 This is consistent with the most dominant contribution to AOD in the area, which was sea salt  
 834 and dust (Fig. 10b). The back-trajectories were from East Asia around the same latitude as  
 835 Taiwan (Fig. 10d). That area, at that time, had increased AOD in general from sulfate and dust

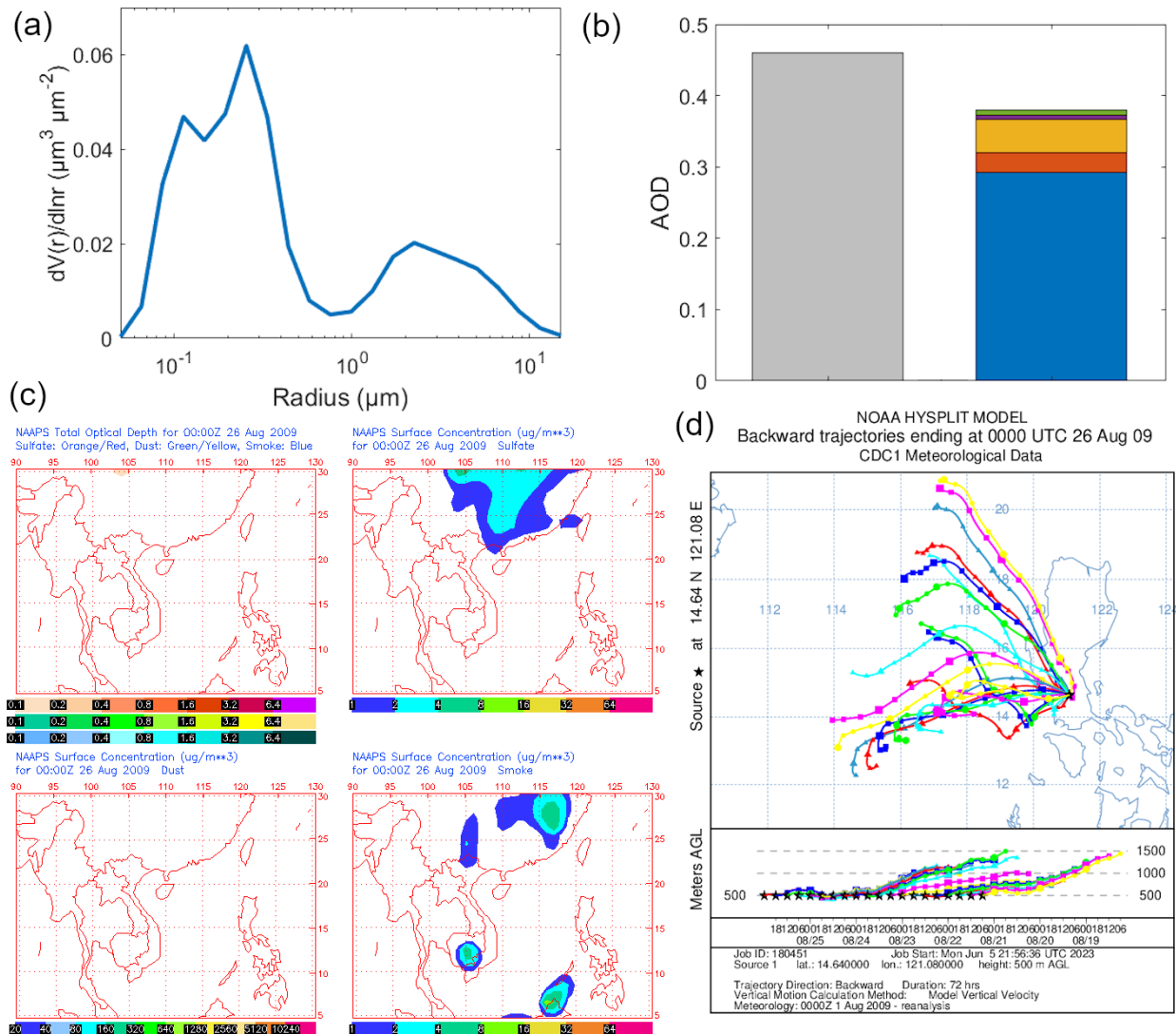
836 (Fig. 10c). The AOD from both AERONET and MERRA-2 (Fig. 10b) are lower than 0.3 (the  
 837 AOD threshold for dust in other studies, Table 2) because of the long distance from the source  
 838 (thousands of kilometers). The dust and sulfate seemed to have been transported to Metro Manila  
 839 from East Asia based on the NAAPS sulfate and dust surface concentrations (Fig. 10c).  
 840



841 **Figure 10:** Case study of long-range transport (dust) around 24-25 March 2018. (a) AERONET  
 842 VSD at (blue) 23:23 UTC, (b) AOD from AERONET (gray: AOD at 500 nm) and MERRA-2  
 843 hourly (green: black carbon, violet: dust, yellow: sea salt, orange: organic carbon, blue: sulfate)  
 844 compositional contributions to AOD (550 nm) closest in time to 23:23 UTC, (c) NAAPS maps of  
 845 total and compositional hourly AOD (orange/red: sulfate, green/yellow: dust, blue: smoke) and  
 846 sulfate, dust, and smoke surface concentrations at 00:00 UTC on March 25, and (d) HYSPLIT  
 847 seven-day back-trajectories arriving at Manila Observatory at 23:00 UTC.  
 848

849  
 850 3.4.3 Cloud Processing

851 Sulfate dominated the AOD (Fig. 11b) for this case on 26 August 2009 in the area around Metro  
852 Manila. This along with its VSD exhibiting a second peak (Fig. 11a) in the accumulation mode  
853 make it very similar to the cloud processing cluster (cluster 5). Sulfate has been known to be  
854 enhanced through chemical productions in clouds and is used as a signature for cloud processing  
855 (Barth et al., 2000; Ervens et al., 2018). Aqueous production of sulfate is significant in areas with  
856 sources and clouds (Barth et al., 2000), and this case study has both. Aside from the high sulfate  
857 contribution to AOD, the cloud fraction (Aqua/MODIS, Terra/MODIS, Fig. S3) is very high  
858 (~100%) in the area of the back-trajectories (Fig. 11d). Interestingly, there is no regional AOD  
859 elevation observed in the NAAPS maps (Fig. 11c) for this time. There are increased surface  
860 smoke and sulfate levels in East Asia as well as southwest of the Philippines, and though the  
861 back-trajectories do show a northeastward direction, they do not reach far enough into mainland  
862 East Asia. It is possible that even while there are known regional sources of sulfate in Southeast  
863 Asia (Smith et al., 2011; Li et al., 2017), this case could be local to the Philippines. There is in  
864 fact a large power plant northwest of Metro Manila (Jamora et al., 2020).  
865

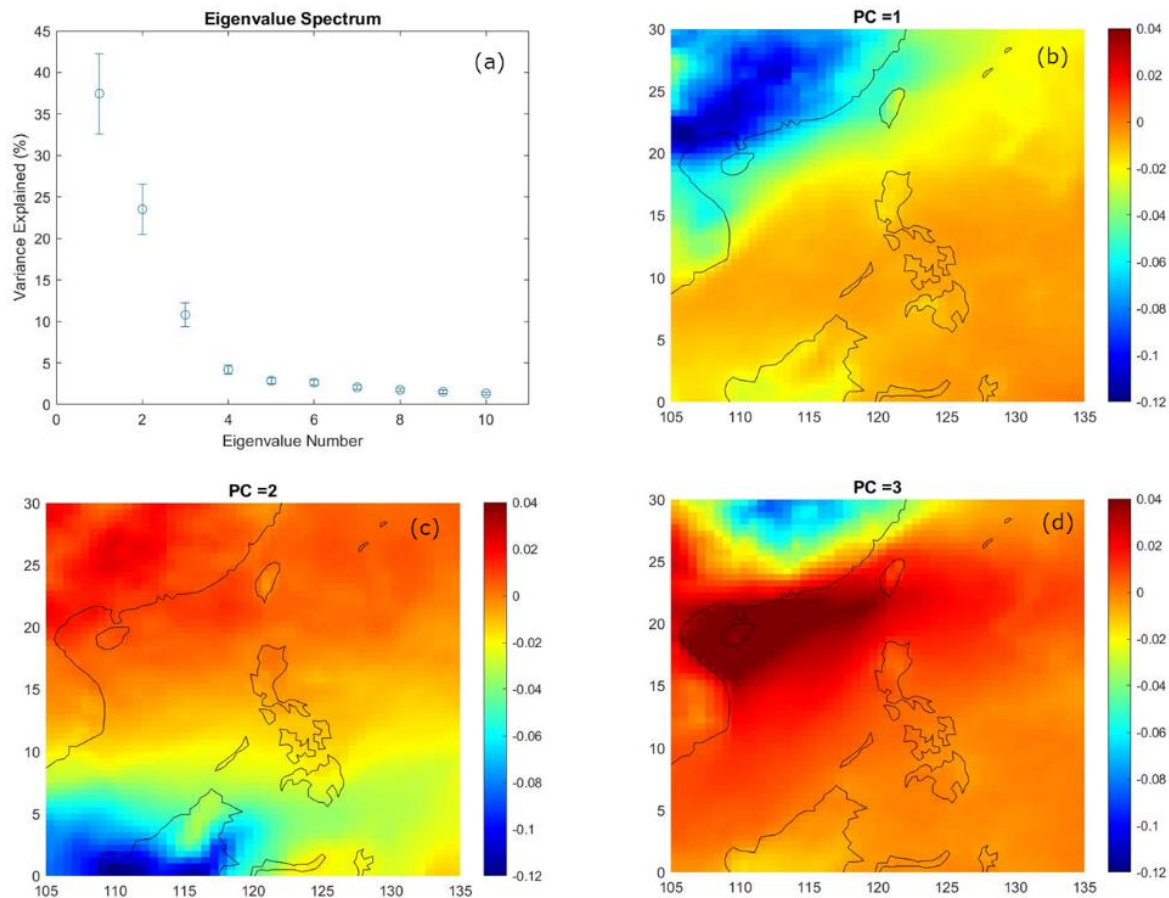


866  
 867 **Figure 11:** Case study of cloud processing on 26 August 2009. (a) AERONET VSDs at 00:18  
 868 UTC, (b) AOD from AERONET (gray: median AOD at 500 nm) and MERRA-2 hourly (green:  
 869 black carbon, violet: dust, yellow: sea salt, orange: organic carbon, blue: sulfate) compositional  
 870 contributions to AOD (550 nm) closest in time to 00:18 UTC, (c) NAAPS maps of total and  
 871 compositional hourly AOD and contributions and smoke surface concentrations at 00:00 UTC,  
 872 and (d) HYSPLIT seven-day back-trajectories arriving at Manila Observatory at 00:00 UTC.  
 873

### 874 3.5 EOF Analysis of AOD in Southeast Asia

876 The air masses in Metro Manila are influenced by regional sources which were identified  
 877 through EOF analysis of AOD. Three principal components (PC, Fig. 12) explained most of the  
 878 data variance (73.77%) (Fig. 12a) and were all well-separated from each other and are therefore  
 879 most probably the major distinct aerosol particle sources in the region. They will be the focus of  
 880 the subsequent discussion.





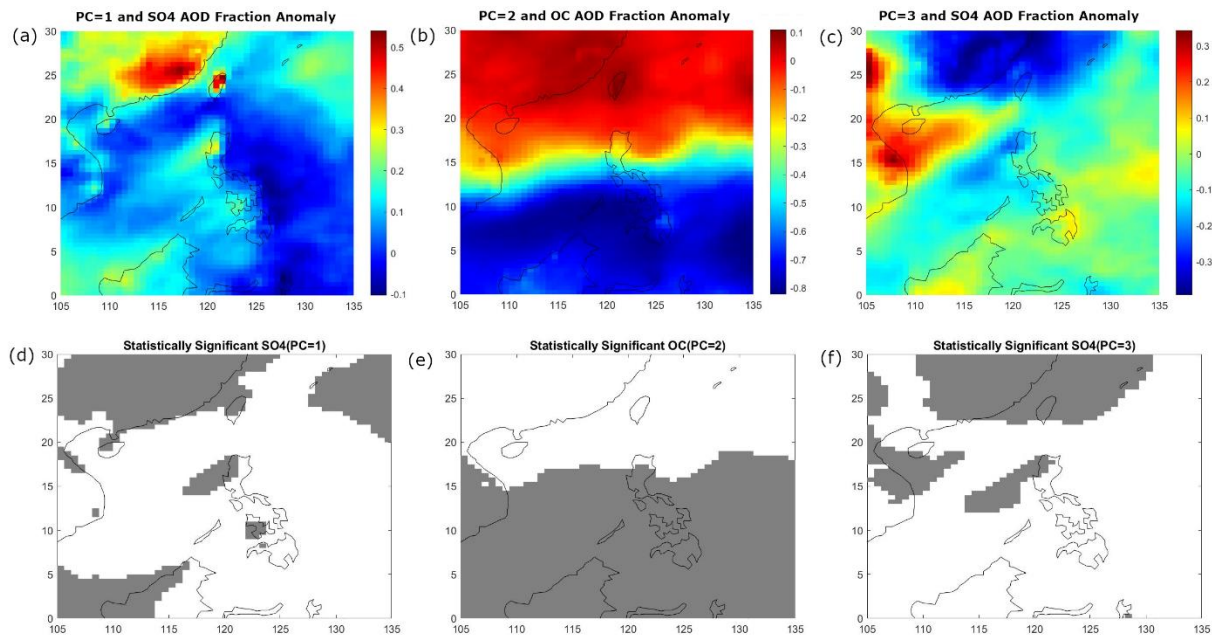
881  
 882 **Figure 12:** Results of the singular value decomposition. (a) Eigenvalue spectrum of the first ten  
 883 eigenvalues, (b-d) maps of the coefficients of regression AOD anomalies onto the first three  
 884 principal components.

885 The first PC explains 37.46% of the data variance (Fig. 12a) and, based on the map of the  
 886 regression coefficients (Fig. 12b), separates mainland East Asia from the Philippines and  
 887 Indonesia. East Asia is a globally recognized source for high AOD (Li et al., 2013), and its  
 888 contribution to particles in Southeast Asia possibly corresponds to the first PC. The second PC  
 889 explains 25.51% of the data variance (Fig. 12a) and separates southern Southeast Asia from  
 890 northern Southeast Asia at around 15°N (Fig. 12c). Southern Southeast Asia is a known regional  
 891 source of aerosol particles due to biomass burning (Cohen et al., 2017) and could be associated  
 892 with the second PC. The third PC explains 10.80% of the data variance (Fig. 12a) and separates  
 893 northern East Asia from southern East Asia mainland and the rest of Southeast Asia (Fig. 12d).

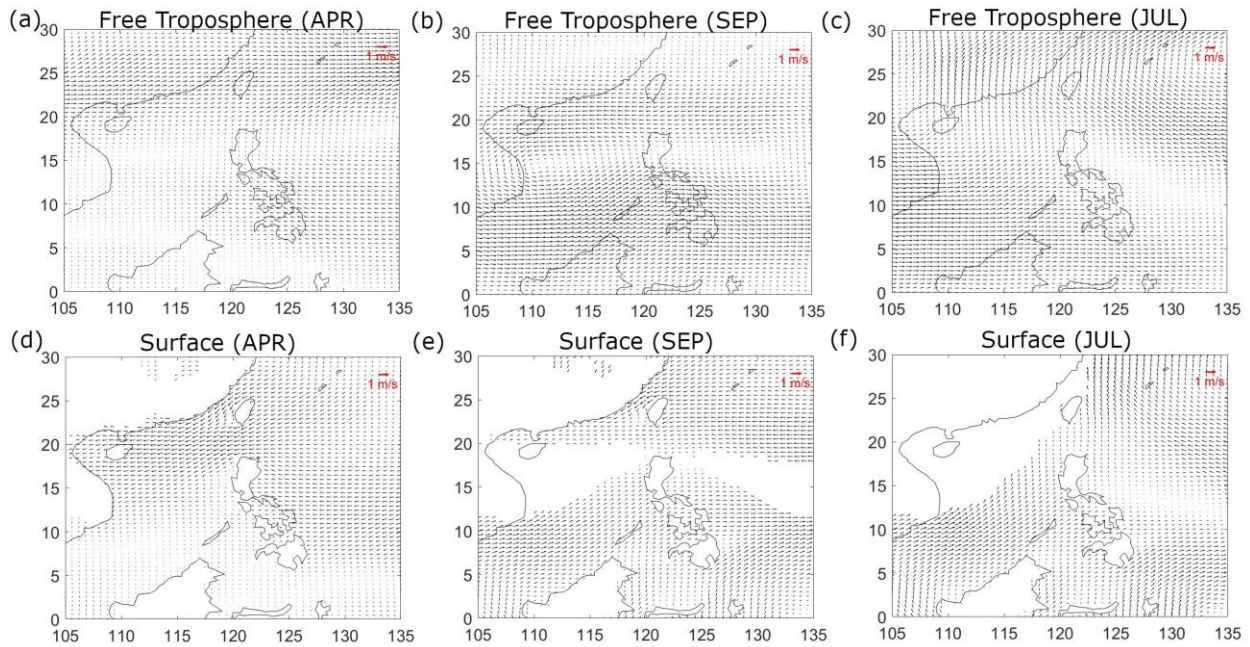
894 To gain confidence in the association of the PCs with their sources, we present correlation maps  
 895 between the first three PCs to the fractional contributions of sulfate and organic carbon to AOD  
 896 for the entire dataset.

897 The correlation maps of the first PC and the sulfate contribution to AOD (Fig. 13a and 13d)  
 898 show high and statistically significant correlations (gray areas) in mainland East Asia and  
 899 Taiwan, parts of western Philippines and Borneo, which are the probable sulfate sources. Clues  
 900 from the mean monthly wind vector maps in April (Fig. 14a and 14d) and mean monthly AOD in

901 either March or April (Fig. S3c or S3e) most resembling the features of regression map of the  
 902 first PC (Fig. 12b) and the PC time series peaking in March (Fig. S4) together suggest that the  
 903 first PC may be associated with air masses that are present around March or April. Emissions  
 904 sources and meteorology that are dominant during the peak dates in the PC time series offer  
 905 clues to the attribution of each PC. The Southeast Asia region and the Philippines is influenced  
 906 by the monsoon systems (Coronas, 1920; Matsumoto et al., 2020) and February to March is the  
 907 time when the winds are transitioning from the northeasterly to easterly. The first PC could be  
 908 affected by the easterly winds, which are dominant around March when its PC values peaked.  
 909 The higher-level winds (free troposphere) (Fig. 14a) in April are from the west in mainland East  
 910 Asia and are from the east in the Philippines and it is possible that the different wind regimes are  
 911 distinguishing the sulfate sources in East Asia and the Philippines and beyond. Sulfate is a  
 912 known product of industry in East Asia (Smith et al., 2011; Li et al., 2017) while the West Luzon  
 913 and West Visayas islands have large power plants (Jamora et al., 2020).



914 **Figure 13:** Correlation coefficients of principal components with (a/c) sulfate AOD fraction and  
 915 (b) organic carbon AOD fraction. Statistically significant (90%, d-f) areas are shaded gray.  
 916



917 **Figure 14:** Monthly averaged winds for (a & d) April, (b & e) September, and (c & f) July from  
 918 MERRA-2 at (725 hPa, a-c) the free troposphere approximate and at (1000 hPa, d-f) the surface.  
 919

920 The correlation maps of the second PC and the OC contribution to AOD (Fig. 13b and 13e) show  
 921 high and statistically significant correlations from 0°N to 15°N. The large magnitude of the  
 922 correlation coefficient (gray areas in Fig. 13b) stands out in southern Southeast Asia and is the  
 923 potential OC source. In this case, it is known that Indonesia is a major source of biomass burning  
 924 during its fire season (Glover and Jessup, 1998), and thus the local significance established in the  
 925 southern Southeast Asia is most likely due to the Indonesia biomass burning source. The burning  
 926 season in Indonesia is from August to October, and that is the same time when the AOD values  
 927 peak in the area (Fig. S3h, S3i, and S3j), as well as the peak of the second PC in the time series  
 928 (Fig. S4). Winds are usually from the southwest and west due to the southwest monsoon from  
 929 September to October, when the second PC peaked, and thus the second PC may be related to the  
 930 southwest monsoon. During the same time the surface and free troposphere mean monthly winds  
 931 (Fig. 14b and 14e) are from the southwest (in the general direction of Indonesia) towards the  
 932 south portion of Southeast Asia and thus corroborate the observation that the second PC may be  
 933 highlighting the regional effect of the Indonesia forest fires. Of interest is the line of separation  
 934 of the northern and southern Southeast Asia in the principal component that is within the area of  
 935 the monsoon trough (Wang et al., 2007). This line is also evident in the surface and the free  
 936 troposphere maps where the southwest winds from the area of Indonesia meet the easterlies in  
 937 north Southeast Asia (Fig. 14b and 14e) and which thus appears to be limiting the dispersion of  
 938 the biomass burning emissions to southern Southeast Asia.

939 The third PC was also well correlated to the sulfate AOD fraction though, compared to the first  
 940 PC correlation maps, there were distinctions between the northern and southern East Asia  
 941 regions (Fig. 13c and 13f). The local Philippine source still came out in the correlation maps as a  
 942 significant source. It was not clear from the PC time series (Fig. S4), which showed peaks in the  
 943 third PC in February, how the dates were related to the PC profile. The free troposphere winds in  
 944 July (Fig. 14c), as well as the AOD monthly mean map in July (Fig. 14c), however, showed

945 more similarities to the third PC regression map. Both showed a delineation between the  
946 northern East Asia and southern East Asia (including Hong Kong) features. Mean winds (Fig.  
947 14c) in the free troposphere are from the west, due to the southwest monsoon, in the area around  
948 the Philippines, and they were from the northeast in north Southeast Asia. The interface of the  
949 winds is within the approximate location of the monsoon trough in July (Wang et al., 2007), and  
950 it is thus possible that the monsoon trough is causing the separation of the sulfate sources. This  
951 could be investigated further. The monsoon trough has been noted to scavenge aerosol particles  
952 from southern Southeast Asia (Reid et al., 2013). It is evident from the analysis that meteorology  
953 affects the transport and processing of aerosol particles in region which along with local sources  
954 contribute to the aerosol composition in Southeast Asia (Cruz et al., 2019; AzadiAghdam et al.,  
955 2019; Braun et al., 2020; Hilario et al., 2020b; Hilario et al., 2022).

956

#### 957 **4. Conclusion**

958 Metro Manila has both urban and industrial local sources known to contribute to the dominance  
959 of fine mode particles in its air (Cruz et al., 2019). Ten years of AERONET data in Manila  
960 Observatory suggest that aerosol particles in Metro Manila were mixed in size but with a  
961 prevalent fine mode fraction (>50% FMF) throughout the year. Background clean marine aerosol  
962 particles (58% of the time) and fine polluted aerosol particles (20% of the time) were the most  
963 dominant clear sky day sources impacting the atmospheric column over Metro Manila based on  
964 cluster analysis of volume size distributions. The proximity of Metro Manila to the sea, both in  
965 the east and west, along with local sources, transportation being the most prominent, together  
966 contribute to the prevalence of the marine and fine particles. The prevalence of marine particles  
967 could explain the relatively small AOD values in Metro Manila compared to other Southeast  
968 Asian megacities (Reid et al., 2013).

969 Regional sources and meteorology also impact monthly aerosol optical depth trends in Metro  
970 Manila from EOF analysis. Biomass burning from Borneo and Sumatra emerged in the study as  
971 the second most prevalent regional anthropogenic aerosol particle source in Southeast Asia.  
972 Though the monsoon trough limits the dispersion of aerosol particles throughout the entire  
973 Southeast Asia, biomass burning emissions impact southern Southeast Asia including Metro  
974 Manila during the southwest monsoon (July to September). The monsoon winds facilitate the  
975 transport of fine particles during the peak burning season in Borneo and Sumatra (August-  
976 September). This is experienced in Metro Manila as higher than usual aerosol particle loadings  
977 around the same period (August to October). Climatologically, August was also when there were  
978 particles with the greatest fine mode fractions that were relatively absorbing and non-  
979 hygroscopic possibly due to increased organic and elemental carbon fractional contributions.  
980 Though not as strong a source as the Borneo and Sumatra case, the peninsular Southeast Asia  
981 burning season (March-April) also contributed to extreme aerosol particle concentrations over  
982 Metro Manila.

983 High aerosol particle loadings due to transported dust, probably from East Asia, were observed  
984 in Metro Manila during the transition period between the southwest and northeast monsoons and  
985 during the northeast monsoon (December to February). These extreme events are transient  
986 because the lowest median aerosol particle loadings of the year were observed during the  
987 northeast monsoon when annual wind speeds were highest. Particles then were observed to be  
988 largest in diameter, with the greatest coarse fraction contribution, relatively high absorptivity,



989 and most hygroscopicity, compared to other months of the year. This is probably due to  
990 constituents other than soot, especially aged dust (Kim and Park, 2012; Geng et al., 2014) and  
991 sea salt which the northeast winds appear to be bringing in from the general direction of the  
992 Luzon Island and the Philippine Sea (West Pacific Ocean).

993 Cloud processing is one of the cases that were linked to very high aerosol particle loading in  
994 Metro Manila. This is associated with sulfate sources, which appear more localized in nature  
995 because of a power plant nearby. This sulfate source seems to be distinct from the industrial  
996 sulfate air mass from East Asia, which is the most dominant regional aerosol particle source in  
997 Southeast Asia (Li et al., 2013). Winds appear to limit the mixing of this notable East Asia air  
998 mass with local industrial sources in the region including the Philippines and Indonesia.

999 The formation of cloud systems in Southeast Asia is complex due to intersecting large- and  
1000 small-scale mechanisms. Additionally, the interaction of particles and clouds in Southeast Asia is  
1001 not yet well understood. In Metro Manila, both topography and meteorology affect aerosol  
1002 particle distribution (Cruz et al., 2023). This baseline study on the aerosol particle characteristics  
1003 in Metro Manila and in regional Southeast Asia shows how meteorology impacts varied aerosol  
1004 particle sources (e.g., sulfate, elemental carbon, and organic carbon) and their distribution in the  
1005 region. This can help in mitigating aerosol particle sources in the region and in the deepening of  
1006 the understanding of the relationship of aerosol particles, meteorology, and clouds.  
1007

#### 1008 **Data availability**

1009 Aerosol Robotic Network (AERONET) (2020), Version 3 Direct Sun Algorithm, Site: Manila  
1010 Observatory, Philippines, Accessed: [**28 September 2020**], [https://aeronet.gsfc.nasa.gov/cgi-  
1011 bin/webtool\\_aod\\_v3?stage=3&region=Asia&state=Philippines&site=Manila\\_Observatory&plac  
1012 e\\_code=10&if\\_polarized=0](https://aeronet.gsfc.nasa.gov/cgi-bin/webtool_aod_v3?stage=3&region=Asia&state=Philippines&site=Manila_Observatory&place_code=10&if_polarized=0)

1013 Aerosol Robotic Network (AERONET) (2020), Version 3 Direct Sun and Inversion Algorithm,  
1014 Site: Manila Observatory, Philippines, Accessed: [**28 September 2020**],  
1015 [https://aeronet.gsfc.nasa.gov/cgi-  
1016 bin/webtool\\_inv\\_v3?stage=3&region=Asia&state=Philippines&site=Manila\\_Observatory&place  
1017 \\_code=10&if\\_polarized=0](https://aeronet.gsfc.nasa.gov/cgi-bin/webtool_inv_v3?stage=3&region=Asia&state=Philippines&site=Manila_Observatory&place_code=10&if_polarized=0)

1018 Multi-angle Imaging SpectroRadiometer (MISR) Jet Propulsion Laboratory (2018), Level 3  
1019 Component Global Aerosol product in netCDF format covering a month V004, Accessed: [**22  
1020 November 2021**], <https://search.earthdata.nasa.gov/>

1021 Global Modeling and Assimilation Office (GMAO) (2015), MERRA-2 inst3\_3d\_asm\_Np: 3d,3-  
1022 Hourly, Instantaneous, Pressure-Level, Assimilation, Assimilated Meteorological Fields V5.12.4,  
1023 Greenbelt, MD, USA, Goddard Earth Sciences Data and Information Services Center (GES  
1024 DISC), Accessed: [**10 March 2021**], <https://doi.org/10.5067/QBZ6MG944HW0>

1025 Global Modeling and Assimilation Office (GMAO) (2015), MERRA-2 tavg1\_2d\_flux\_Nx: 2d,1-  
1026 Hourly, Time-Averaged, Single-Level, Assimilation, Surface Flux Diagnostics V5.12.4,  
1027 Greenbelt, MD, USA, Goddard Earth Sciences Data and Information Services Center (GES  
1028 DISC), Accessed: [**10 March 2021**], <https://doi.org/10.5067/7MCPBJ41Y0K6>

1029 Global Modeling and Assimilation Office (GMAO) (2015), MERRA-2 tavg1\_2d\_csp\_Nx: 2d,1-  
1030 Hourly, Time-averaged, Single-Level, Assimilation, COSP Satellite Simulator V5.12.4,  
1031 Greenbelt, MD, USA, Goddard Earth Sciences Data and Information Services Center (GES  
1032 DISC), Accessed: [**13 July 2021**], <https://doi.org/10.5067/H0VVAD8F6MX5>

1033 Nguyen, P., E.J. Shearer, H. Tran, M. Ombadi, N. Hayatbini, T. Palacios, P. Huynh, G.  
1034 Updegraff, K. Hsu, B. Kuligowski, W.S. Logan, and S. Sorooshian, The CHRS Data Portal, an  
1035 easily accessible public repository for PERSIANN global satellite precipitation data, Nature  
1036 Scientific Data, Vol. 6, Article 180296, 2019, Accessed: [**11 March 2021**],  
1037 <https://doi.org/10.1038/sdata.2018.296>

1038

#### 1039 **Author contributions**

1040 GRL and AS designed the experiment. NL, SNU, GRL, GFG, HJO, JBS, and MTC, carried out  
1041 various aspects of the data collection. GRL, AS, JBS, MOC, MRH, CC, and LDG conducted  
1042 analysis and interpretation of the data. GRL prepared the manuscript draft with contributions  
1043 from the coauthors. AFA, LDG, MRH, GRL, and AS reviewed and edited the manuscript. AS  
1044 led the management and funding acquisition. All authors approved the final version of the  
1045 manuscript.

1046

#### 1047 **Competing interests**

1048 We declare that Armin Sorooshian is a member of the editorial board of Atmospheric Chemistry  
1049 and Physics. The peer-review process was guided by an independent editor, and the authors have  
1050 also no other competing interests to declare.

1051

#### 1052 **Acknowledgements**

1053 The authors acknowledge support from NASA grant 80NSSC18K0148 in support of the NASA  
1054 CAMP<sup>2</sup>Ex project, in addition to ONR grant N00014-21-1-2115. We acknowledge the US Naval  
1055 Research Laboratory for providing the AERONET instrument. We acknowledge the use of  
1056 imagery from the NASA Worldview application (<https://worldview.earthdata.nasa.gov>), part of  
1057 the NASA Earth Observing System Data and Information System (EOSDIS).

1058

#### 1059 **References:**

1060 AERONET Inversion Products (Version 3):

1061 [https://aeronet.gsfc.nasa.gov/new\\_web/Documents/Inversion\\_products\\_for\\_V3.pdf](https://aeronet.gsfc.nasa.gov/new_web/Documents/Inversion_products_for_V3.pdf), access: June  
1062 25, 2021, 2019.

1063 Alas, H. D., Müller, T., Birmili, W., Kecorius, S., Cambaliza, M. O., Simpas, J. B. B., Cayetano,  
1064 M., Weinhold, K., Vallar, E., and Galvez, M. C.: Spatial characterization of black carbon mass  
1065 concentration in the atmosphere of a southeast asian megacity: an air quality case study for  
1066 Metro Manila, Philippines, Aerosol Air Qual. Res., 18, 2301-2317,  
1067 <https://doi.org/10.4209/aaqr.2017.08.0281>, 2018.

- 1068 Aldhaif, A. M., Lopez, D. H., Dadashazar, H., and Sorooshian, A.: Sources, frequency, and  
 1069 chemical nature of dust events impacting the United States East Coast, *Atmos. Environ.*, 231,  
 1070 117456, <https://doi.org/10.1016/j.atmosenv.2020.117456>, 2020.
- 1071 Aldhaif, A. M., Lopez, D. H., Dadashazar, H., Painemal, D., Peters, A. J., and Sorooshian, A.:  
 1072 An Aerosol Climatology and Implications for Clouds at a Remote Marine Site: Case Study Over  
 1073 Bermuda, *J. Geophys. Res.- Atmos.*, 126, e2020JD034038,  
 1074 <https://doi.org/10.1029/2020JD034038>, 2021.
- 1075 Alizadeh-Choobari, O., and Gharaylou, M.: Aerosol impacts on radiative and microphysical  
 1076 properties of clouds and precipitation formation, *Atmos. Res.*, 185, 53-64,  
 1077 <https://doi.org/10.1016/j.atmosres.2016.10.021>, 2017.
- 1078 Amnuaylojaroen, T.: Air Pollution Modeling in Southeast Asia—An Overview, *Vegetation Fires  
 1079 and Pollution in Asia*, 531-544, [https://doi.org/10.1007/978-3-031-29916-2\\_31](https://doi.org/10.1007/978-3-031-29916-2_31), 2023.
- 1080 Ångström, A.: On the atmospheric transmission of sun radiation and on dust in the air,  
 1081 *Geografiska Annaler*, 11, 156-166, 1929.
- 1082 Arthur, D., and Vassilvitskii, S.: k-means++: The advantages of careful seeding, Stanford, 2006.
- 1083 AzadiAghdam, M., Braun, R. A., Edwards, E.-L., Bañaga, P. A., Cruz, M. T., Betito, G.,  
 1084 Cambaliza, M. O., Dadashazar, H., Lorenzo, G. R., and Ma, L.: On the nature of sea salt aerosol  
 1085 at a coastal megacity: Insights from Manila, Philippines in Southeast Asia, *Atmos. Environ.*, 216,  
 1086 116922, <https://doi.org/10.1016/j.atmosenv.2019.116922>, 2019.
- 1087 Bagtasa, G.: Contribution of tropical cyclones to rainfall in the Philippines, *Journal of Climate*,  
 1088 30, 3621-3633, <https://doi.org/10.1175/JCLI-D-16-0150.1>, 2017.
- 1089 Bañares, E. N., Narisma, G. T. T., Simpas, J. B. B., Cruz, F. A. T., Lorenzo, G. R. H.,  
 1090 Cambaliza, M. O. L., and Coronel, R. C.: Seasonal and diurnal variations of observed convective  
 1091 rain events in metro Manila, Philippines, *Atmos. Res.*, 105646,  
 1092 <https://doi.org/10.1016/j.atmosres.2021.105646>, 2021.
- 1093 Barth, M., Rasch, P., Kiehl, J., Benkovitz, C., and Schwartz, S.: Sulfur chemistry in the National  
 1094 Center for Atmospheric Research Community Climate Model: Description, evaluation, features,  
 1095 and sensitivity to aqueous chemistry, *J. Geophys. Res.- Atmos.*, 105, 1387-1415,  
 1096 <https://doi.org/10.1029/1999JD900773>, 2000.
- 1097 Bautista VII, A. T., Pabroa, P. C. B., Santos, F. L., Racho, J. M. D., and Quirit, L. L.:  
 1098 Carbonaceous particulate matter characterization in an urban and a rural site in the Philippines,  
 1099 *Atmospheric Pollution Research*, 5, 245-252, <https://doi.org/10.5094/APR.2014.030>, 2014.
- 1100 Bergstrom, R. W., Russell, P. B., and Hignett, P.: Wavelength dependence of the absorption of  
 1101 black carbon particles: Predictions and results from the TARFOX experiment and implications  
 1102 for the aerosol single scattering albedo, *J. Atmos. Sci.*, 59, 567-577,  
 1103 [https://doi.org/10.1175/1520-0469\(2002\)059<0567:WDOTAO>2.0.CO;2](https://doi.org/10.1175/1520-0469(2002)059<0567:WDOTAO>2.0.CO;2), 2002.

- 1104 Bergstrom, R. W., Pilewskie, P., Schmid, B., and Russell, P. B.: Estimates of the spectral aerosol  
 1105 single scattering albedo and aerosol radiative effects during SAFARI 2000, *J. Geophys. Res.-*  
 1106 *Atmos.*, 108, <https://doi.org/10.1029/2002JD002435>, 2003.
- 1107 Bergstrom, R. W., Pilewskie, P., Russell, P. B., Redemann, J., Bond, T. C., Quinn, P. K., and  
 1108 Sierau, B.: Spectral absorption properties of atmospheric aerosols, *Atmos. Chem. Phys.*, 7, 5937-  
 1109 5943, <https://doi.org/10.5194/acp-7-5937-2007>, 2007.
- 1110 Bi, J., Huang, J., Hu, Z., Holben, B., and Guo, Z.: Investigating the aerosol optical and radiative  
 1111 characteristics of heavy haze episodes in Beijing during January of 2013, *J. Geophys. Res.-*  
 1112 *Atmos.*, 119, 9884-9900, <https://doi.org/10.1002/2014JD021757>, 2014.
- 1113 Björnsson, H., and Venegas, S.: A manual for EOF and SVD analyses of climatic data, CCGCR  
 1114 Report, 97, 112-134, 1997.
- 1115 Bohren, C. F., and Clothiaux, E. E.: Fundamentals of atmospheric radiation: an introduction with  
 1116 400 problems, John Wiley & Sons, 2006.
- 1117 Braun, R. A., Aghdam, M. A., Bañaga, P. A., Betito, G., Cambaliza, M. O., Cruz, M. T.,  
 1118 Lorenzo, G. R., MacDonald, A. B., Simpas, J. B., and Stahl, C.: Long-range aerosol transport  
 1119 and impacts on size-resolved aerosol composition in Metro Manila, Philippines, *Atmos. Chem.*  
 1120 *Phys.*, 20, 2387-2405, <https://doi.org/10.5194/acp-20-2387-2020>, 2020.
- 1121 Buchard, V., Randles, C., Da Silva, A., Darmenov, A., Colarco, P., Govindaraju, R., Ferrare, R.,  
 1122 Hair, J., Beyersdorf, A., and Ziemba, L.: The MERRA-2 aerosol reanalysis, 1980 onward. Part  
 1123 II: Evaluation and case studies, *Journal of Climate*, 30, 6851-6872, [https://doi.org/10.1175/JCLI-](https://doi.org/10.1175/JCLI-D-16-0613.1)  
 1124 [D-16-0613.1](https://doi.org/10.1175/JCLI-D-16-0613.1), 2017.
- 1125 Cahyono, W. E., Setyawati, W., Hamdi, S., Cholianawati, N., Kombara, P. Y., and Sari, W. J.:  
 1126 Observations of aerosol optical properties during tropical forest fires in Indonesia, *Materials*  
 1127 *Today: Proceedings*, 63, S445-S450, <https://doi.org/10.1016/j.matpr.2022.04.113>, 2022.
- 1128 Caido, N. G., Ong, P. M., Rempillo, O., Galvez, M. C., and Vallar, E.: Spatiotemporal analysis  
 1129 of MODIS aerosol optical depth data in the Philippines from 2010 to 2020, *Atmosphere*, 13, 939,  
 1130 <https://doi.org/10.3390/atmos13060939>, 2022.
- 1131 Chang, C.-P., Wang, Z., McBride, J., and Liu, C.-H.: Annual cycle of Southeast Asia—Maritime  
 1132 Continent rainfall and the asymmetric monsoon transition, *Journal of climate*, 18, 287-301,  
 1133 <https://doi.org/10.1175/JCLI-3257.1>, 2005.
- 1134 Che, H., Xia, X., Zhu, J., Wang, H., Wang, Y., Sun, J., Zhang, X., and Shi, G.: Aerosol optical  
 1135 properties under the condition of heavy haze over an urban site of Beijing, China, *Environ. Sci.*  
 1136 *Pollut. R.*, 22, 1043-1053, <https://doi.org/10.1007/s11356-014-3415-5>, 2015.
- 1137 Chen, Q., McGowan, S., Gouramanis, C., Fong, L., Balasubramanian, R., and Taylor, D.:  
 1138 Rapidly rising transboundary atmospheric pollution from industrial and urban sources in  
 1139 Southeast Asia and its implications for regional sustainable development, *Environ. Res. Lett.*, 15,  
 1140 1040a1045, <https://doi.org/10.1088/1748-9326/abb5ce>, 2020.



1141 Choi, M., Lim, H., Kim, J., Lee, S., Eck, T. F., Holben, B. N., Garay, M. J., Hyer, E. J., Saide, P.  
1142 E., and Liu, H.: Validation, comparison, and integration of GOCI, AHI, MODIS, MISR, and  
1143 VIIRS aerosol optical depth over East Asia during the 2016 KORUS-AQ campaign, *Atmos.*  
1144 *Meas. Tech.*, 12, 4619-4641, <https://doi.org/10.5194/amt-12-4619-2019>, 2019.

1145 Cohen, J. B.: Quantifying the occurrence and magnitude of the Southeast Asian fire climatology,  
1146 *Environmental Research Letters*, 9, 114018, <https://dx.doi.org/10.1088/1748-9326/9/11/114018>,  
1147 2014.

1148 Cohen, J. B., Lecoœur, E., and Hui Loong Ng, D.: Decadal-scale relationship between  
1149 measurements of aerosols, land-use change, and fire over Southeast Asia, *Atmos. Chem. Phys.*,  
1150 17, 721-743, <https://doi.org/10.5194/acp-17-721-2017>, 2017.

1151 Coronas, J.: *The Climate and Weather of the Philippines, 1903-1918*, by Rev. José Coronas. SJ,  
1152 Chief, Meteorological Division, Weather Bureau, Manila Observatory, Manila.: Bureau of  
1153 Printing, 1920.

1154 Crosbie, E., Sorooshian, A., Monfared, N. A., Shingler, T., and Esmaili, O.: A multi-year aerosol  
1155 characterization for the greater Tehran area using satellite, surface, and modeling data,  
1156 *Atmosphere*, 5, 178-197, <https://doi.org/10.3390/atmos5020178>, 2014.

1157 Crosbie, E., Ziemba, L. D., Shook, M. A., Robinson, C. E., Winstead, E. L., Thornhill, K. L.,  
1158 Braun, R. A., MacDonald, A. B., Stahl, C., and Sorooshian, A.: Measurement report: Closure  
1159 analysis of aerosol–cloud composition in tropical maritime warm convection, *Atmos. Chem.*  
1160 *Phys.*, 22, 13269-13302, <https://doi.org/10.5194/acp-22-13269-2022>, 2022.

1161 Cruz, F., Narisma, G. T., Villafuerte II, M. Q., Chua, K. C., and Olaguera, L. M.: A  
1162 climatological analysis of the southwest monsoon rainfall in the Philippines, *Atmos. Res.*, 122,  
1163 609-616, <https://doi.org/10.1016/j.atmosres.2012.06.010>, 2013.

1164 Cruz, M. T., Bañaga, P. A., Betito, G., Braun, R. A., Stahl, C., Aghdam, M. A., Cambaliza, M.  
1165 O., Dadashazar, H., Hilario, M. R., Lorenzo, G. R., Ma, L., MacDonald, A. B., Pabroa, C., Yee,  
1166 J. R., Simpas, J. B., and Sorooshian, A.: Size-resolved composition and morphology of  
1167 particulate matter during the southwest monsoon in Metro Manila, Philippines, *Atmos. Chem.*  
1168 *Phys.*, 19, 10675–10696, <https://doi.org/10.5194/acp-19-10675-2019>, 2019.

1169 Cruz, M. T., Simpas, J. B., Sorooshian, A., Betito, G., Cambaliza, M. O. L., Collado, J. T.,  
1170 Eloranta, E. W., Holz, R., Topacio, X. G. V., and Del Socorro, J.: Impacts of regional wind  
1171 circulations on aerosol pollution and planetary boundary layer structure in Metro Manila,  
1172 Philippines, *Atmos. Environ.*, 293, 119455, <https://doi.org/10.1016/j.atmosenv.2022.119455>,  
1173 2023.

1174 Deep, A., Pandey, C. P., Nandan, H., Singh, N., Yadav, G., Joshi, P., Purohit, K., and Bhatt, S.:  
1175 Aerosols optical depth and Ångström exponent over different regions in Garhwal Himalaya,  
1176 India, *Environmental Monitoring and Assessment*, 193, 324, [https://doi.org/10.1007/s10661-021-](https://doi.org/10.1007/s10661-021-09048-4)  
1177 09048-4, 2021.

1178 Di Girolamo, L., Holz, R., Reid, J., Tanelli, S., van den Heever, S., Narsma, G., and Simpas, J.:  
1179 Cloud and aerosol monsoonal processes-Philippines experiment (CAMP2Ex), NASA White  
1180 Paper, 2015.

1181 Diner, D. J., Di Girolamo, L., and Nolin, A.: Preface to the MISR special issue, *Remote Sens.*  
1182 *Environ.*, 107, 1, <https://doi.org/10.1016/j.rse.2006.11.001>, 2007.

1183 Dong, X., and Fu, J. S.: Understanding interannual variations of biomass burning from  
1184 Peninsular Southeast Asia, part II: Variability and different influences in lower and higher  
1185 atmosphere levels, *Atmospheric Environment*, 115, 9-18,  
1186 <https://doi.org/10.1016/j.atmosenv.2015.05.052>, 2015.

1187 Dorado, S. V., Holdsworth, J. L., Lagrosas, N. C., Villarin, J. R., Narisma, G., Ellis, J., and  
1188 Perez, R.: Characterization of urban atmosphere of Manila with lidar, filter sampling, and  
1189 radiosonde, *Lidar Remote Sensing for Industry and Environment Monitoring*, 2001, 591-598,

1190 Dubovik, O., Holben, B., Kaufman, Y., Yamasoe, M., Smirnov, A., Tanré, D., and Slutsker, I.:  
1191 Single-scattering albedo of smoke retrieved from the sky radiance and solar transmittance  
1192 measured from ground, *J. Geophys. Res.- Atmos.*, 103, 31903-31923,  
1193 <https://doi.org/10.1029/98JD02276>, 1998.

1194 Dubovik, O., and King, M. D.: A flexible inversion algorithm for retrieval of aerosol optical  
1195 properties from Sun and sky radiance measurements, *J. Geophys. Res.- Atmos.*, 105, 20673-  
1196 20696, <https://doi.org/10.1029/2000JD900282>, 2000.

1197 Dubovik, O., Holben, B., Eck, T. F., Smirnov, A., Kaufman, Y. J., King, M. D., Tanré, D., and  
1198 Slutsker, I.: Variability of absorption and optical properties of key aerosol types observed in  
1199 worldwide locations, *J. Atmos. Sci.*, 59, 590-608, [https://doi.org/10.1175/1520-  
1200 0469\(2002\)059<0590:VOAAOP>2.0.CO;2](https://doi.org/10.1175/1520-0469(2002)059<0590:VOAAOP>2.0.CO;2), 2002.

1201 Eck, T., Holben, B., Reid, J., O'Neill, N., Schafer, J., Dubovik, O., Smirnov, A., Yamasoe, M.,  
1202 and Artaxo, P.: High aerosol optical depth biomass burning events: A comparison of optical  
1203 properties for different source regions, *Geophys. Res. Lett.*, 30,  
1204 <https://doi.org/10.1029/2003GL017861>, 2003.

1205 Eck, T., Holben, B., Dubovik, O., Smirnov, A., Goloub, P., Chen, H., Chatenet, B., Gomes, L.,  
1206 Zhang, X. Y., and Tsay, S. C.: Columnar aerosol optical properties at AERONET sites in central  
1207 eastern Asia and aerosol transport to the tropical mid-Pacific, *J. Geophys. Res.- Atmos.*, 110,  
1208 <https://doi.org/10.1029/2004JD005274>, 2005.

1209 Eck, T., Holben, B., Reid, J., Mukelabai, M., Piketh, S., Torres, O., Jethva, H., Hyer, E., Ward,  
1210 D., and Dubovik, O.: A seasonal trend of single scattering albedo in southern African biomass-  
1211 burning particles: Implications for satellite products and estimates of emissions for the world's  
1212 largest biomass-burning source, *J. Geophys. Res.- Atmos.*, 118, 6414-6432,  
1213 <https://doi.org/10.1002/jgrd.50500>, 2013.

1214 Eck, T. F., Holben, B., Reid, J., Dubovik, O., Smirnov, A., O'Neill, N., Slutsker, I., and Kinne, S.:  
1215 Wavelength dependence of the optical depth of biomass burning, urban, and desert dust aerosols,  
1216 *J. Geophys. Res.- Atmos.*, 104, 31333-31349, <https://doi.org/10.1029/1999JD900923>, 1999.

1217 Eck, T. F., Holben, B. N., Reid, J., Giles, D., Rivas, M., Singh, R. P., Tripathi, S., Bruegge, C.,  
1218 Platnick, S., and Arnold, G.: Fog-and cloud-induced aerosol modification observed by the  
1219 Aerosol Robotic Network (AERONET), *J. Geophys. Res.- Atmos.*, 117,  
1220 <https://doi.org/10.1029/2011JD016839>, 2012.

1221 Edwards, E.-L., Reid, J. S., Xian, P., Burton, S. P., Cook, A. L., Crosbie, E. C., Fenn, M. A.,  
1222 Ferrare, R. A., Freeman, S. W., and Hair, J. W.: Assessment of NAAPS-RA performance in  
1223 Maritime Southeast Asia during CAMP 2 Ex, *Atmospheric Chemistry and Physics*, 22, 12961-  
1224 12983, <https://doi.org/10.5194/acp-22-12961-2022>, 2022.

1225 Ervens, B., Sorooshian, A., Aldhaif, A. M., Shingler, T., Crosbie, E., Ziemba, L., Campuzano-  
1226 Jost, P., Jimenez, J. L., and Wisthaler, A.: Is there an aerosol signature of chemical cloud  
1227 processing?, *Atmos. Chem. Phys.*, 18, 16099-16119, <https://doi.org/10.5194/acp-18-16099-2018>,  
1228 2018.

1229 Faloon, I.: Sulfur processing in the marine atmospheric boundary layer: A review and critical  
1230 assessment of modeling uncertainties, *Atmos. Environ.*, 43, 2841-2854,  
1231 <https://doi.org/10.1016/j.atmosenv.2009.02.043>, 2009.

1232 Feingold, G.: Modeling of the first indirect effect: Analysis of measurement requirements,  
1233 *Geophys. Res. Lett.*, 30, <https://doi.org/10.1029/2003GL017967>, 2003.

1234 Flores, J.: Climate of the Philippines, *Climates of the Northern and Eastern Asia*, 159-213, 1969.

1235 Formenti, P., Andreae, M. O., and Lelieveld, J.: Measurements of aerosol optical depth above  
1236 3570 m asl in the North Atlantic free troposphere: results from ACE-2, *Tellus B*, 52, 678-693,  
1237 <https://doi.org/10.1034/j.1600-0889.2000.00006.x>, 2000.

1238 Foth, A., Kanitz, T., Engelmann, R., Baars, H., Radenz, M., Seifert, P., Barja, B., Fromm, M.,  
1239 Kalesse, H., and Ansmann, A.: Vertical aerosol distribution in the southern hemispheric  
1240 midlatitudes as observed with lidar in Punta Arenas, Chile (53.2° S and 70.9° W), during  
1241 ALPACA, *Atmospheric Chemistry and Physics*, 19, 6217-6233, <https://doi.org/10.5194/acp-19-6217-2019>, 2019.

1243 Garay, M. J., Bull, M. A., Nastan, A. M., Witek, M. L., Seidel, F. C., Diner, D. J., Kahn, R. A.,  
1244 Limbacher, J. A., and Kalashnikova, O. V.: Data Product Specification for the MISR Level 2  
1245 Aerosol Product, Jet Propulsion Laboratory, California Institute of Technology. JPL D-100649.  
1246 [https://asdc.larc.nasa.gov/documents/misr/DPS\\_AEROSOL\\_V023.20180125.pdf](https://asdc.larc.nasa.gov/documents/misr/DPS_AEROSOL_V023.20180125.pdf), 2018.

1247 Gautam, R., Hsu, N. C., Eck, T. F., Holben, B. N., Janjai, S., Jantarach, T., Tsay, S.-C., and Lau,  
1248 W. K.: Characterization of aerosols over the Indochina peninsula from satellite-surface  
1249 observations during biomass burning pre-monsoon season, *Atmos. Environ.*, 78, 51-59,  
1250 <https://doi.org/10.1016/j.atmosenv.2012.05.038>, 2013.

- 1251 Gelaro, R., McCarty, W., Suárez, M. J., Todling, R., Molod, A., Takacs, L., Randles, C. A.,  
 1252 Darmenov, A., Bosilovich, M. G., and Reichle, R.: The modern-era retrospective analysis for  
 1253 research and applications, version 2 (MERRA-2), *J. Climate*, 30, 5419-5454,  
 1254 <https://doi.org/10.1175/JCLI-D-16-0758.1>, 2017.
- 1255 Geng, H., Hwang, H., Liu, X., Dong, S., and Ro, C.-U.: Investigation of aged aerosols in size-  
 1256 resolved Asian dust storm particles transported from Beijing, China, to Incheon, Korea, using  
 1257 low-Z particle EPMA, *Atmos. Chem. Phys.*, 14, 3307-3323, [https://doi.org/10.5194/acp-14-](https://doi.org/10.5194/acp-14-3307-2014)  
 1258 3307-2014, 2014.
- 1259 Giles, D. M., Holben, B. N., Eck, T. F., Sinyuk, A., Smirnov, A., Slutsker, I., Dickerson, R.,  
 1260 Thompson, A., and Schafer, J.: An analysis of AERONET aerosol absorption properties and  
 1261 classifications representative of aerosol source regions, *J. Geophys. Res.- Atmos.*, 117,  
 1262 <https://doi.org/10.1029/2012JD018127>, 2012.
- 1263 Giles, D. M., Sinyuk, A., Sorokin, M. G., Schafer, J. S., Smirnov, A., Slutsker, I., Eck, T. F.,  
 1264 Holben, B. N., Lewis, J. R., and Campbell, J. R.: Advancements in the Aerosol Robotic Network  
 1265 (AERONET) Version 3 database—automated near-real-time quality control algorithm with  
 1266 improved cloud screening for Sun photometer aerosol optical depth (AOD) measurements,  
 1267 *Atmos. Meas. Tech.*, 12, 169-209, <https://doi.org/10.5194/amt-12-169-2019>, 2019.
- 1268 Glover, D., and Jessup, T.: The Indonesian fires and haze of 1997: the economic toll, *Economy*  
 1269 *and Environment Program for SE Asia (EEPSEA)* Singapore and the World Wildlife Fund  
 1270 (WWF) Indonesia, Jakarta, 1998.
- 1271 Guyon, P., Boucher, O., Graham, B., Beck, J., Mayol-Bracero, O. L., Roberts, G. C., Maenhaut,  
 1272 W., Artaxo, P., and Andreae, M. O.: Refractive index of aerosol particles over the Amazon  
 1273 tropical forest during LBA-EUSTACH 1999, *J. Aerosol Sci.*, 34, 883-907,  
 1274 [https://doi.org/10.1016/S0021-8502\(03\)00052-1](https://doi.org/10.1016/S0021-8502(03)00052-1), 2003.
- 1275 Harenda, K. M., Markowicz, K. M., Poczta, P., Stachlewska, I. S., Bojanowski, J. S., Czernecki,  
 1276 B., McArthur, A., Schuetemeyer, D., and Chojnicki, B. H.: Estimation of the effects of aerosol  
 1277 optical properties on peatland production in Rzecin, Poland, *Agricultural and Forest*  
 1278 *Meteorology*, 316, 108861, <https://doi.org/10.1016/j.agrformet.2022.108861>, 2022.
- 1279 Hartley, W. S., and Hobbs, P. V.: An aerosol model and aerosol-induced changes in the clear-sky  
 1280 albedo off the east coast of the United States, *J. Geophys. Res.- Atmos.*, 106, 9733-9748,  
 1281 <https://doi.org/10.1029/2001JD900025>, 2001.
- 1282 Haywood, J., and Boucher, O.: Estimates of the direct and indirect radiative forcing due to  
 1283 tropospheric aerosols: A review, *Rev. Geophys.*, 38, 513-543,  
 1284 <https://doi.org/10.1029/1999RG000078>, 2000.
- 1285 Hendrickson, B. N., Brooks, S. D., Thornton, D. C., Moore, R. H., Crosbie, E., Ziemba, L. D.,  
 1286 Carlson, C. A., Baetge, N., Mirrielees, J. A., and Alsante, A. N.: Role of sea surface microlayer  
 1287 properties in cloud formation, *Frontiers in Marine Science*, 7, 596225,  
 1288 <https://doi.org/10.3389/fmars.2020.596225>, 2021.

1289 Herber, A., Thomason, L. W., Gernandt, H., Leiterer, U., Nagel, D., Schulz, K. H., Kaptur, J.,  
1290 Albrecht, T., and Notholt, J.: Continuous day and night aerosol optical depth observations in the  
1291 Arctic between 1991 and 1999, *J. Geophys. Res.- Atmos.*, 107, AAC 6-1-AAC 6-13,  
1292 <https://doi.org/10.1029/2001JD000536>, 2002.

1293 Hilario, M. R. A., Cruz, M. T., Bañaga, P. A., Betito, G., Braun, R. A., Stahl, C., Cambaliza, M.  
1294 O., Lorenzo, G. R., MacDonald, A. B., AzadiAghdam, M., Pabroa, P. C., Yee, J. R., Simpas, J.  
1295 B., and Sorooshian, A.: Characterizing weekly cycles of particulate matter in a coastal megacity:  
1296 The importance of a seasonal, size-resolved, and chemically-speciated analysis, *J. Geophys.*  
1297 *Res.- Atmos.*, 125, e2020JD032614, <https://doi.org/10.1029/2020JD032614>, 2020a.

1298 Hilario, M. R. A., Cruz, M. T., Cambaliza, M. O. L., Reid, J. S., Xian, P., Simpas, J. B.,  
1299 Lagrosas, N. D., Uy, S. N. Y., Cliff, S., and Zhao, Y.: Investigating size-segregated sources of  
1300 elemental composition of particulate matter in the South China Sea during the 2011 Vasco  
1301 cruise, *Atmos. Chem. Phys.*, 20, 1255-1276, <https://doi.org/10.5194/acp-20-1255-2020>, 2020b.

1302 Hilario, M. R. A., Crosbie, E., Shook, M., Reid, J. S., Cambaliza, M. O. L., Simpas, J. B. B.,  
1303 Ziemba, L., DiGangi, J. P., Diskin, G. S., and Nguyen, P.: Measurement report: Long-range  
1304 transport patterns into the tropical northwest Pacific during the CAMP 2 Ex aircraft campaign:  
1305 chemical composition, size distributions, and the impact of convection, *Atmos. Chem. Phys.*, 21,  
1306 3777-3802, <https://doi.org/10.5194/acp-21-3777-2021>, 2021a.

1307 Hilario, M. R. A., Olaguera, L. M., Narisma, G. T., and Matsumoto, J.: Diurnal characteristics of  
1308 summer precipitation over Luzon Island, Philippines, *Asia-Pacific Journal of Atmospheric*  
1309 *Sciences*, 57, 573-585, <https://doi.org/10.1007/s13143-020-00214-1>, 2021b.

1310 Hilario, M. R. A., Bañaga, P. A., Betito, G., Braun, R. A., Cambaliza, M. O., Cruz, M. T.,  
1311 Lorenzo, G. R., MacDonald, A. B., Pabroa, P. C., and Simpas, J. B.: Stubborn aerosol: why  
1312 particulate mass concentrations do not drop during the wet season in Metro Manila, Philippines,  
1313 *Environmental Science: Atmospheres*, 2, 1428-1437, <https://doi.org/10.1039/D2EA00073C>,  
1314 2022.

1315 Hogan, T. F., Liu, M., Ridout, J. A., Peng, M. S., Whitcomb, T. R., Ruston, B. C., Reynolds, C.  
1316 A., Eckermann, S. D., Moskaitis, J. R., and Baker, N. L.: The navy global environmental model,  
1317 *Oceanography*, 27, 116-125, <https://doi.org/10.5670/oceanog.2014.73>, 2014.

1318 Holben, B. N., Eck, T. F., Slutsker, I. a., Tanre, D., Buis, J., Setzer, A., Vermote, E., Reagan, J.  
1319 A., Kaufman, Y., and Nakajima, T.: AERONET—A federated instrument network and data  
1320 archive for aerosol characterization, *Remote Sens. Environ.*, 66, 1-16,  
1321 [https://doi.org/10.1016/S0034-4257\(98\)00031-5](https://doi.org/10.1016/S0034-4257(98)00031-5), 1998.

1322 Holben, B. N., Tanre, D., Smirnov, A., Eck, T., Slutsker, I., Abuhassan, N., Newcomb, W.,  
1323 Schafer, J., Chatenet, B., and Lavenu, F.: An emerging ground-based aerosol climatology:  
1324 Aerosol optical depth from AERONET, *J. Geophys. Res.- Atmos.*, 106, 12067-12097,  
1325 <https://doi.org/10.1029/2001JD900014>, 2001.

- 1326 Hong, Y., and Di Girolamo, L.: Cloud phase characteristics over Southeast Asia from A-Train  
1327 satellite observations, *Atmos. Chem. Phys.*, 20, 8267-8291, [https://doi.org/10.5194/acp-20-8267-](https://doi.org/10.5194/acp-20-8267-2020)  
1328 2020, 2020.
- 1329 Hong, Y., and Di Girolamo, L.: An overview of aerosol properties in clear and cloudy sky based  
1330 on CALIPSO observations, *Earth and Space Science*, 9, e2022EA002287,  
1331 <https://doi.org/10.1029/2022EA002287>, 2022.
- 1332 Hoppel, W., Frick, G., Fitzgerald, J., and Larson, R.: Marine boundary layer measurements of  
1333 new particle formation and the effects nonprecipitating clouds have on aerosol size distribution,  
1334 *J. Geophys. Res.- Atmos.*, 99, 14443-14459, <https://doi.org/10.1029/94JD00797>, 1994.
- 1335 Huang, C., Li, J., Sun, W., Chen, Q., Mao, Q.-J., and Yuan, Y.: Long-Term Variation  
1336 Assessment of Aerosol Load and Dominant Types over Asia for Air Quality Studies Using  
1337 Multi-Sources Aerosol Datasets, *Remote Sensing*, 13, 3116, <https://doi.org/10.3390/rs13163116>,  
1338 2021.
- 1339 Hyer, E. J., Reid, J. S., Prins, E. M., Hoffman, J. P., Schmidt, C. C., Miettinen, J. I., and Giglio,  
1340 L.: Patterns of fire activity over Indonesia and Malaysia from polar and geostationary satellite  
1341 observations, *Atmos. Res.*, 122, 504-519, <https://doi.org/10.1016/j.atmosres.2012.06.011>, 2013.
- 1342 Jamora, J. B., Gudia, S. E. L., Go, A. W., Giduquio, M. B., and Loretero, M. E.: Potential CO2  
1343 reduction and cost evaluation in use and transport of coal ash as cement replacement: A case in  
1344 the Philippines, *Waste Manage.*, 103, 137-145, <https://doi.org/10.1016/j.wasman.2019.12.026>,  
1345 2020.
- 1346 Jose, S., Gharai, B., Niranjana, K., and Rao, P.: Investigation on seasonal variations of aerosol  
1347 properties and its influence on radiative effect over an urban location in central India, *Atmos.*  
1348 *Environ.*, 133, 41-48, <https://doi.org/10.1016/j.atmosenv.2016.03.029>, 2016.
- 1349 Kaskaoutis, D., Kosmopoulos, P., Kambezidis, H., and Nastos, P.: Aerosol climatology and  
1350 discrimination of different types over Athens, Greece, based on MODIS data, *Atmos. Environ.*,  
1351 41, 7315-7329, <https://doi.org/10.1016/j.atmosenv.2007.05.017>, 2007.
- 1352 Kaskaoutis, D., Badarinath, K., Kumar Kharol, S., Rani Sharma, A., and Kambezidis, H.:  
1353 Variations in the aerosol optical properties and types over the tropical urban site of Hyderabad,  
1354 India, *Journal of Geophysical Research: Atmospheres*, 114,  
1355 <https://doi.org/10.1029/2009JD012423>, 2009.
- 1356 Kiely, L., Spracklen, D. V., Wiedinmyer, C., Conibear, L., Reddington, C. L., Archer-Nicholls,  
1357 S., Lowe, D., Arnold, S. R., Knute, C., and Khan, M. F.: New estimate of particulate emissions  
1358 from Indonesian peat fires in 2015, *Atmospheric Chemistry and Physics*, 19, 11105-11121,  
1359 <https://doi.org/10.5194/acp-19-11105-2019>, 2019.
- 1360 Kim, J.-S., and Park, K.: Atmospheric aging of Asian dust particles during long range transport,  
1361 *Aerosol Sci. Tech.*, 46, 913-924, <https://doi.org/10.1080/02786826.2012.680984>, 2012.

- 1362 Kirchstetter, T. W., Novakov, T., and Hobbs, P. V.: Evidence that the spectral dependence of  
1363 light absorption by aerosols is affected by organic carbon, *J. Geophys. Res.- Atmos.*, 109,  
1364 <https://doi.org/10.1029/2004JD004999>, 2004.
- 1365 Koven, C. D., and Fung, I.: Inferring dust composition from wavelength-dependent absorption in  
1366 Aerosol Robotic Network (AERONET) data, *J. Geophys. Res.- Atmos.*, 111,  
1367 <https://doi.org/10.1029/2005JD006678>, 2006.
- 1368 Kudo, R., Nishizawa, T., and Aoyagi, T.: Vertical profiles of aerosol optical properties and the  
1369 solar heating rate estimated by combining sky radiometer and lidar measurements, *Atmos. Meas.*  
1370 *Tech.*, 9, 3223-3243, <https://doi.org/10.5194/amt-9-3223-2016>, 2016.
- 1371 Kumar, K. R., Sivakumar, V., Reddy, R. R., Gopal, K. R., and Adesina, A. J.: Identification and  
1372 classification of different aerosol types over a subtropical rural site in Mpumalanga, South  
1373 Africa: seasonal variations as retrieved from the AERONET Sunphotometer, *Aerosol Air Qual.*  
1374 *Res.*, 14, 108-123, <https://doi.org/10.4209/aaqr.2013.03.0079>, 2014.
- 1375 Kumar, K. R., Yin, Y., Sivakumar, V., Kang, N., Yu, X., Diao, Y., Adesina, A. J., and Reddy,  
1376 R.: Aerosol climatology and discrimination of aerosol types retrieved from MODIS, MISR and  
1377 OMI over Durban (29.88 S, 31.02 E), South Africa, *Atmos. Environ.*, 117, 9-18,  
1378 <https://doi.org/10.1016/j.atmosenv.2015.06.058>, 2015.
- 1379 Kuttippurath, J., and Raj, S.: Two decades of aerosol observations by AATSR, MISR, MODIS  
1380 and MERRA-2 over India and Indian Ocean, *Remote Sens. Environ.*, 257, 112363,  
1381 <https://doi.org/10.1016/j.rse.2021.112363>, 2021.
- 1382 Lee, H.-H., Iraqui, O., Gu, Y., Yim, S. H.-L., Chulakadabba, A., Tonks, A. Y.-M., Yang, Z., and  
1383 Wang, C.: Impacts of air pollutants from fire and non-fire emissions on the regional air quality in  
1384 Southeast Asia, *Atmos. Chem. Phys.*, 18, 6141-6156, <https://doi.org/10.5194/acp-18-6141-2018>,  
1385 2018.
- 1386 Lee, J., Kim, J., Song, C., Kim, S., Chun, Y., Sohn, B., and Holben, B.: Characteristics of aerosol  
1387 types from AERONET sunphotometer measurements, *Atmospheric Environment*, 44, 3110-  
1388 3117, <https://doi.org/10.1016/j.atmosenv.2010.05.035>, 2010.
- 1389 Li, G., Bei, N., Cao, J., Huang, R., Wu, J., Feng, T., Wang, Y., Liu, S., Zhang, Q., and Tie, X.: A  
1390 possible pathway for rapid growth of sulfate during haze days in China, *Atmos. Chem. Phys.*, 17,  
1391 3301-3316, <https://doi.org/10.5194/acp-17-3301-2017>, 2017.
- 1392 Li, J., Carlson, B. E., and Lacis, A. A.: Application of spectral analysis techniques in the  
1393 intercomparison of aerosol data: 1. An EOF approach to analyze the spatial-temporal variability  
1394 of aerosol optical depth using multiple remote sensing data sets, *J. Geophys. Res.- Atmos.*, 118,  
1395 8640-8648, <https://doi.org/10.1002/jgrd.50686>, 2013.
- 1396 Li, Z., Niu, F., Fan, J., Liu, Y., Rosenfeld, D., and Ding, Y.: Long-term impacts of aerosols on  
1397 the vertical development of clouds and precipitation, *Nat. Geosci.*, 4, 888-894,  
1398 <https://doi.org/10.1038/ngeo1313>, 2011.

1399 Lin, N.-H., Sayer, A. M., Wang, S.-H., Loftus, A. M., Hsiao, T.-C., Sheu, G.-R., Hsu, N. C.,  
1400 Tsay, S.-C., and Chantara, S.: Interactions between biomass-burning aerosols and clouds over  
1401 Southeast Asia: Current status, challenges, and perspectives, *Environ. Pollut.*, 195, 292-307,  
1402 <https://doi.org/10.1016/j.envpol.2014.06.036>, 2014.

1403 Lloyd, S.: Least squares quantization in PCM, *IEEE T. Inform. Theory*, 28, 129-137,  
1404 <https://doi.org/10.1109/TIT.1982.1056489>, 1982.

1405 Lynch, P., Reid, J. S., Westphal, D. L., Zhang, J., Hogan, T. F., Hyer, E. J., Curtis, C. A., Hegg,  
1406 D. A., Shi, Y., and Campbell, J. R.: An 11-year global gridded aerosol optical thickness  
1407 reanalysis (v1. 0) for atmospheric and climate sciences, *Geosci. Model Dev.*, 9,  
1408 <https://doi.org/10.5194/gmd-9-1489-2016>, 2016.

1409 Markowicz, K., Zawadzka-Manko, O., Lisok, J., Chilinski, M., and Xian, P.: The impact of  
1410 moderately absorbing aerosol on surface sensible, latent, and net radiative fluxes during the  
1411 summer of 2015 in Central Europe, *Journal of Aerosol Science*, 151, 105627,  
1412 <https://doi.org/10.1016/j.jaerosci.2020.105627>, 2021.

1413 Matsumoto, J., Olaguera, L. M. P., Nguyen-Le, D., Kubota, H., and Villafuerte, M. Q.:  
1414 Climatological seasonal changes of wind and rainfall in the Philippines, *Int. J. Climatol.*, 40,  
1415 4843-4857, <https://doi.org/10.1002/joc.6492>, 2020.

1416 Mims III, F. M.: A 30-Year Climatology (1990–2020) of Aerosol Optical Depth and Total  
1417 Column Water Vapor and Ozone over Texas, *Bulletin of the American Meteorological Society*,  
1418 103, E101-E109, <https://doi.org/10.1175/BAMS-D-21-0010.1>, 2022.

1419 Moosmüller, H., and Sorensen, C.: Small and large particle limits of single scattering albedo for  
1420 homogeneous, spherical particles, *J. Quant. Spectrosc. Ra.*, 204, 250-255,  
1421 <https://doi.org/10.1016/j.jqsrt.2017.09.029>, 2018.

1422 Mora, M., Braun, R. A., Shingler, T., and Sorooshian, A.: Analysis of remotely sensed and  
1423 surface data of aerosols and meteorology for the Mexico Megalopolis Area between 2003 and  
1424 2015, *J. Geophys. Res.- Atmos.*, 122, 8705-8723, <https://doi.org/10.1002/2017JD026739>, 2017.

1425 Nakata, M., Mukai, S., and Yasumoto, M.: Seasonal and regional characteristics of aerosol  
1426 pollution in east and southeast Asia, *Frontiers in Environmental Science*, 6, 29,  
1427 <https://doi.org/10.3389/fenvs.2018.00029>, 2018.

1428 Fires and Smoke in Borneo: [https://earthobservatory.nasa.gov/images/40182/fires-and-smoke-in-](https://earthobservatory.nasa.gov/images/40182/fires-and-smoke-in-borneo)  
1429 borneo), 2009.

1430 Nguyen, P., Shearer, E. J., Tran, H., Ombadi, M., Hayatbini, N., Palacios, T., Huynh, P.,  
1431 Braithwaite, D., Updegraff, G., and Hsu, K.: The CHRS Data Portal, an easily accessible public  
1432 repository for PERSIANN global satellite precipitation data, *Scientific Data*, 6, 1-10,  
1433 <https://doi.org/10.1038/sdata.2018.296>, 2019a.

1434 Nguyen, T. T., Pham, H. V., Lasko, K., Bui, M. T., Laffly, D., Jourdan, A., and Bui, H. Q.:  
1435 Spatiotemporal analysis of ground and satellite-based aerosol for air quality assessment in the



1436 Southeast Asia region, *Environmental Pollution*, 255, 113106,  
1437 <https://doi.org/10.1016/j.envpol.2019.113106>, 2019b.

1438 North, G. R., Bell, T. L., Cahalan, R. F., and Moeng, F. J.: Sampling errors in the estimation of  
1439 empirical orthogonal functions, *Mon. Weather Rev.*, 110, 699-706, [https://doi.org/10.1175/1520-0493\(1982\)110<0699:SEITEO>2.0.CO;2](https://doi.org/10.1175/1520-0493(1982)110<0699:SEITEO>2.0.CO;2), 1982.

1441 O'Neill, N., Eck, T., Smirnov, A., Holben, B., and Thulasiraman, S.: Spectral discrimination of  
1442 coarse and fine mode optical depth, *J. Geophys. Res.- Atmos.*, 108,  
1443 <https://doi.org/10.1029/2002JD002975>, 2003.

1444 Oanh, N. K., Upadhyay, N., Zhuang, Y.-H., Hao, Z.-P., Murthy, D., Lestari, P., Villarin, J.,  
1445 Chengchua, K., Co, H., and Dung, N.: Particulate air pollution in six Asian cities: Spatial and  
1446 temporal distributions, and associated sources, *Atmospheric environment*, 40, 3367-3380,  
1447 <https://doi.org/10.1016/j.atmosenv.2006.01.050>, 2006.

1448 Oanh, N. T. K., Permadi, D. A., Hopke, P. K., Smith, K. R., Dong, N. P., and Dang, A. N.:  
1449 Annual emissions of air toxics emitted from crop residue open burning in Southeast Asia over  
1450 the period of 2010–2015, *Atmos. Environ.*, 187, 163-173,  
1451 <https://doi.org/10.1016/j.atmosenv.2018.05.061>, 2018.

1452 Ong, H. J. J., Lagrosas, N., Uy, S. N., Gacal, G. F. B., Dorado, S., Tobias Jr, V., and Holben, B.:  
1453 Determination of Monthly Aerosol Types in Manila Observatory and Notre Dame of Marbel  
1454 University from Aerosol Robotic Network (AERONET) measurements, AGU Fall Meeting  
1455 Abstracts, 2016, A54E-03,

1456 Pace, G., Sarra, A. d., Meloni, D., Piacentino, S., and Chamard, P.: Aerosol optical properties at  
1457 Lampedusa (Central Mediterranean). 1. Influence of transport and identification of different  
1458 aerosol types, *Atmos. Chem. Phys.*, 6, 697-713, <https://doi.org/10.5194/acp-6-697-2006>, 2006.

1459 Pandolfi, M., Alados-Arboledas, L., Alastuey, A., Andrade, M., Angelov, C., Artiñano, B.,  
1460 Backman, J., Baltensperger, U., Bonasoni, P., and Bukowiecki, N.: A European aerosol  
1461 phenomenology–6: scattering properties of atmospheric aerosol particles from 28 ACTRIS sites,  
1462 *Atmos. Chem. Phys.*, 18, 7877-7911, <https://doi.org/10.5194/acp-18-7877-2018>, 2018.

1463 Petters, M. D., Carrico, C. M., Kreidenweis, S. M., Prenni, A. J., DeMott, P. J., Collett Jr, J. L.,  
1464 and Moosmüller, H.: Cloud condensation nucleation activity of biomass burning aerosol, *J.*  
1465 *Geophys. Res.- Atmos.*, 114, <https://doi.org/10.1029/2009JD012353>, 2009.

1466 Plymale, N. T., Szekely, J. E., and Rubinstein, A. H.: Statistical Cluster Analysis of Global  
1467 Aerosol Optical Depth for Simplified Atmospheric Modeling, *J. Appl. Meteorol. Clim.*,  
1468 <https://doi.org/10.1175/JAMC-D-21-0150.1>, 2021.

1469 PSA: Highlights of the Philippine population 2015 census of population, Philippine Statistics  
1470 Authority, 2016.

- 1471 Qi, Y., Ge, J., and Huang, J.: Spatial and temporal distribution of MODIS and MISR aerosol  
1472 optical depth over northern China and comparison with AERONET, Chinese science bulletin,  
1473 58, 2497-2506, <https://doi.org/10.1007/s11434-013-5678-5>, 2013.
- 1474 Ramage, C. S.: Monsoon meteorology, Academic Press, New York, 1971.
- 1475 Randles, C., Da Silva, A., Buchard, V., Colarco, P., Darmenov, A., Govindaraju, R., Smirnov,  
1476 A., Holben, B., Ferrare, R., and Hair, J.: The MERRA-2 aerosol reanalysis, 1980 onward. Part I:  
1477 System description and data assimilation evaluation, *J. Climate*, 30, 6823-6850,  
1478 <https://doi.org/10.1175/JCLI-D-16-0609.1>, 2017.
- 1479 Reid, J., Koppmann, R., Eck, T., and Eleuterio, D.: A review of biomass burning emissions part  
1480 II: intensive physical properties of biomass burning particles, *Atmos. Chem. Phys.*, 5, 799-825,  
1481 <https://doi.org/10.5194/acp-5-799-2005>, 2005.
- 1482 Reid, J., Xian, P., Hyer, E., Flatau, M., Ramirez, E., Turk, F., Sampson, C., Zhang, C., Fukada,  
1483 E., and Maloney, E.: Multi-scale meteorological conceptual analysis of observed active fire  
1484 hotspot activity and smoke optical depth in the Maritime Continent, *Atmos. Chem. Phys.*, 12,  
1485 2117, <https://doi.org/10.5194/acp-12-2117-2012>, 2012.
- 1486 Reid, J., Maring, H., Narisma, G., van den Heever, S., Di Girolamo, L., Ferrare, R., Holz, R.,  
1487 Lawson, P., Mace, G., and Simpas, J.: The coupling between tropical meteorology, aerosol  
1488 lifecycle, convection, and radiation, during the Cloud, Aerosol and Monsoon Processes  
1489 Philippines Experiment (CAMP 2 Ex), *B. Am. Meteorol. Soc.*, [https://doi.org/10.1175/BAMS-](https://doi.org/10.1175/BAMS-D-21-0285.1)  
1490 [D-21-0285.1](https://doi.org/10.1175/BAMS-D-21-0285.1), 2023.
- 1491 Reid, J. S., Hobbs, P. V., Liousse, C., Martins, J. V., Weiss, R. E., and Eck, T. F.: Comparisons  
1492 of techniques for measuring shortwave absorption and black carbon content of aerosols from  
1493 biomass burning in Brazil, *J. Geophys. Res.- Atmos.*, 103, 32031-32040,  
1494 <https://doi.org/10.1029/98JD00773>, 1998.
- 1495 Reid, J. S., Hyer, E. J., Johnson, R. S., Holben, B. N., Yokelson, R. J., Zhang, J., Campbell, J. R.,  
1496 Christopher, S. A., Di Girolamo, L., and Giglio, L.: Observing and understanding the Southeast  
1497 Asian aerosol system by remote sensing: An initial review and analysis for the Seven Southeast  
1498 Asian Studies (7SEAS) program, *Atmos. Res.*, 122, 403-468,  
1499 <https://doi.org/10.1016/j.atmosres.2012.06.005>, 2013.
- 1500 Reid, J. S., Lagrosas, N. D., Jonsson, H. H., Reid, E. A., Sessions, W. R., Simpas, J. B., Uy, S.  
1501 N., Boyd, T., Atwood, S. A., and Blake, D. R.: Observations of the temporal variability in  
1502 aerosol properties and their relationships to meteorology in the summer monsoonal South China  
1503 Sea/East Sea: the scale-dependent role of monsoonal flows, the Madden–Julian Oscillation,  
1504 tropical cyclones, squall lines and cold pools, *Atmos. Chem. Phys.*, 15, 1745-1768,  
1505 <https://doi.org/10.5194/acp-15-1745-2015>, 2015.
- 1506 Rizza, U., Mancinelli, E., Morichetti, M., Passerini, G., and Virgili, S.: Aerosol optical depth of  
1507 the main aerosol species over Italian cities based on the NASA/MERRA-2 model reanalysis,  
1508 *Atmosphere*, 10, 709, <https://doi.org/10.3390/atmos10110709>, 2019.

1509 Rolph, G., Stein, A., and Stunder, B.: Real-time environmental applications and display system:  
1510 READY, *Environ. Modell. Softw.*, 95, 210-228, <https://doi.org/10.1016/j.envsoft.2017.06.025>,  
1511 2017.

1512 Ross, A. D., Holz, R. E., Quinn, G., Reid, J. S., Xian, P., Turk, F. J., and Posselt, D. J.: Exploring  
1513 the first aerosol indirect effect over Southeast Asia using a 10-year collocated MODIS, CALIOP,  
1514 and model dataset, *Atmospheric Chemistry and Physics*, 18, 12747-12764,  
1515 <https://doi.org/10.5194/acp-18-12747-2018>, 2018.

1516 Ross, J. L., Hobbs, P. V., and Holben, B.: Radiative characteristics of regional hazes dominated  
1517 by smoke from biomass burning in Brazil: Closure tests and direct radiative forcing, *J. Geophys.*  
1518 *Res.- Atmos.*, 103, 31925-31941, <https://doi.org/10.1029/97JD03677>, 1998.

1519 Saleh, R., Hennigan, C., McMeeking, G., Chuang, W., Robinson, E., Coe, H., Donahue, N., and  
1520 Robinson, A.: Absorptivity of brown carbon in fresh and photo-chemically aged biomass-  
1521 burning emissions, *Atmos. Chem. Phys.*, 13, 7683-7693, [https://doi.org/10.5194/acp-13-7683-](https://doi.org/10.5194/acp-13-7683-2013)  
1522 2013, 2013.

1523 Schlosser, J. S., Braun, R. A., Bradley, T., Dadashazar, H., MacDonald, A. B., Aldhaif, A. A.,  
1524 Aghdam, M. A., Mardi, A. H., Xian, P., and Sorooshian, A.: Analysis of aerosol composition  
1525 data for western United States wildfires between 2005 and 2015: Dust emissions, chloride  
1526 depletion, and most enhanced aerosol constituents, *J. Geophys. Res.- Atmos.*, 122, 8951-8966,  
1527 <https://doi.org/10.1002/2017JD026547>, 2017.

1528 Schuster, G., Dubovik, O., and Arola, A.: Remote sensing of soot carbon—Part 1: Distinguishing  
1529 different absorbing aerosol species, *Atmos. Chem. Phys.*, 16, 1565-1585,  
1530 <https://doi.org/10.5194/acp-16-1565-2016>, 2016.

1531 Schuster, G. L., Dubovik, O., and Holben, B. N.: Angstrom exponent and bimodal aerosol size  
1532 distributions, *J. Geophys. Res.- Atmos.*, 111, <https://doi.org/10.1029/2005JD006328>, 2006.

1533 Sharma, M., Kaskaoutis, D. G., Singh, R. P., and Singh, S.: Seasonal variability of atmospheric  
1534 aerosol parameters over Greater Noida using ground sunphotometer observations, *Aerosol Air*  
1535 *Qual. Res.*, 14, 608-622, <https://doi.org/10.4209/aaqr.2013.06.0219>, 2014.

1536 Shen, Z., Liu, J., Horowitz, L., Henze, D., Fan, S., Mauzerall, D. L., Lin, J.-T., and Tao, S.:  
1537 Analysis of transpacific transport of black carbon during HIPPO-3: implications for black carbon  
1538 aging, *Atmos. Chem. Phys.*, 14, 6315-6327, <https://doi.org/10.5194/acp-14-6315-2014>, 2014.

1539 Sinyuk, A., Holben, B. N., Eck, T. F., Giles, D. M., Slutsker, I., Korkin, S., Schafer, J. S.,  
1540 Smirnov, A., Sorokin, M., and Lyapustin, A.: The AERONET Version 3 aerosol retrieval  
1541 algorithm, associated uncertainties and comparisons to Version 2, *Atmospheric Measurement*  
1542 *Techniques*, 13, 3375-3411, <https://doi.org/10.5194/amt-13-3375-2020>, 2020.

1543 Smirnov, A., Holben, B. N., Dubovik, O., O'Neill, N. T., Eck, T. F., Westphal, D. L., Goroch, A.  
1544 K., Pietras, C., and Slutsker, I.: Atmospheric aerosol optical properties in the Persian Gulf, *J.*  
1545 *Atmos. Sci.*, 59, 620-634, [https://doi.org/10.1175/1520-](https://doi.org/10.1175/1520-0469(2002)059<0620:AAOPIT>2.0.CO;2)  
1546 0469(2002)059<0620:AAOPIT>2.0.CO;2, 2002.

1547 Smith, S. J., Aardenne, J. v., Klimont, Z., Andres, R. J., Volke, A., and Delgado Arias, S.:  
1548 Anthropogenic sulfur dioxide emissions: 1850–2005, *Atmos. Chem. Phys.*, 11, 1101-1116,  
1549 <https://doi.org/10.5194/acp-11-1101-2011>, 2011.

1550 Sorooshian, A., Wang, Z., Feingold, G., and L'Ecuyer, T. S.: A satellite perspective on cloud  
1551 water to rain water conversion rates and relationships with environmental conditions, *J.*  
1552 *Geophys. Res.- Atmos.*, 118, 6643-6650, <https://doi.org/10.1002/jgrd.50523>, 2013.

1553 Stahl, C., Cruz, M. T., Bañaga, P. A., Betito, G., Braun, R. A., Aghdam, M. A., Cambaliza, M.  
1554 O., Lorenzo, G. R., MacDonald, A. B., and Hilario, M. R. A.: Sources and characteristics of size-  
1555 resolved particulate organic acids and methanesulfonate in a coastal megacity: Manila,  
1556 Philippines, *Atmos. Chem. Phys.*, 20, 15907-15935, <https://doi.org/10.5194/acp-20-15907-2020>,  
1557 2020.

1558 Stahl, C., Crosbie, E., Bañaga, P. A., Betito, G., Braun, R. A., Cainglet, Z. M., Cambaliza, M. O.,  
1559 Cruz, M. T., Dado, J. M., and Hilario, M. R. A.: Total organic carbon and the contribution from  
1560 speciated organics in cloud water: airborne data analysis from the CAMP 2 Ex field campaign,  
1561 *Atmos. Chem. Phys.*, 21, 14109-14129, <https://doi.org/10.5194/acp-21-14109-2021>, 2021.

1562 Stein, A., Draxler, R. R., Rolph, G. D., Stunder, B. J., Cohen, M., and Ngan, F.: NOAA's  
1563 HYSPLIT atmospheric transport and dispersion modeling system, *B. Am. Meteorol. Soc.*, 96,  
1564 2059-2077, <https://doi.org/10.1175/BAMS-D-14-00110.1>, 2015.

1565 Stevens, B., and Feingold, G.: Untangling aerosol effects on clouds and precipitation in a  
1566 buffered system, *Nature*, 461, 607-613, <https://doi.org/10.1038/nature08281>, 2009.

1567 Sullivan, R. C., Levy, R. C., da Silva, A. M., and Pryor, S. C.: Developing and diagnosing  
1568 climate change indicators of regional aerosol optical properties, *Scientific Reports*, 7, 1-13,  
1569 <https://doi.org/10.1038/s41598-017-18402-x>, 2017.

1570 Tao, W. K., Chen, J. P., Li, Z., Wang, C., and Zhang, C.: Impact of aerosols on convective  
1571 clouds and precipitation, *Rev. Geophys.*, 50, <https://doi.org/10.1029/2011RG000369>, 2012.

1572 Tsay, S.-C., Hsu, N. C., Lau, W. K.-M., Li, C., Gabriel, P. M., Ji, Q., Holben, B. N., Welton, E.  
1573 J., Nguyen, A. X., and Janjai, S.: From BASE-ASIA toward 7-SEAS: A satellite-surface  
1574 perspective of boreal spring biomass-burning aerosols and clouds in Southeast Asia,  
1575 *Atmospheric environment*, 78, 20-34, <https://doi.org/10.1016/j.atmosenv.2012.12.013>, 2013.

1576 Van Beelen, A., Roelofs, G., Hasekamp, O., Henzing, J., and Röckmann, T.: Estimation of  
1577 aerosol water and chemical composition from AERONET Sun-sky radiometer measurements at  
1578 Cabauw, the Netherlands, *Atmos. Chem. Phys.*, 14, 5969-5987, <https://doi.org/10.5194/acp-14-5969-2014>, 2014.

1580 Wall, C. J., Norris, J. R., Possner, A., McCoy, D. T., McCoy, I. L., and Lutsko, N. J.: Assessing  
1581 effective radiative forcing from aerosol-cloud interactions over the global ocean, *Proceedings of*  
1582 *the National Academy of Sciences*, 119, e2210481119,  
1583 <https://doi.org/10.1073/pnas.2210481119>, 2022.

1584 Wang, L., Lau, K.-H., Fung, C.-H., and Gan, J.-P.: The relative vorticity of ocean surface winds  
1585 from the QuikSCAT satellite and its effects on the geneses of tropical cyclones in the South  
1586 China Sea, *Tellus A*, 59, 562-569, <https://doi.org/10.1111/j.1600-0870.2007.00249.x>, 2007.

1587 Wang, S.-H., Welton, E. J., Holben, B. N., Tsay, S.-C., Lin, N.-H., Giles, D., Stewart, S. A.,  
1588 Janjai, S., Nguyen, X. A., and Hsiao, T.-C.: Vertical distribution and columnar optical properties  
1589 of springtime biomass-burning aerosols over Northern Indochina during 2014 7-SEAS  
1590 campaign, *Aerosol and Air Quality Research*, 15, 2037-2050,  
1591 <https://doi.org/10.4209/aaqr.2015.05.0310>, 2015.

1592 Wu, M.-c., and Choy, C.-w.: An Observational Study of the Changes in the Intensity and Motion  
1593 of Tropical Cyclones crossing Luzon, *Tropical Cyclone Research and Review*, 4, 95-109,  
1594 <https://doi.org/10.6057/2015TCRRh3.01>, 2016.

1595 Xian, P., Reid, J. S., Atwood, S. A., Johnson, R. S., Hyer, E. J., Westphal, D. L., and Sessions,  
1596 W.: Smoke aerosol transport patterns over the Maritime Continent, *Atmos. Res.*, 122, 469-485,  
1597 <https://doi.org/10.1016/j.atmosres.2012.05.006>, 2013.

1598 Xiao, N., Shi, T., Calder, C. A., Munroe, D. K., Berrett, C., Wolfinbarger, S., and Li, D.: Spatial  
1599 characteristics of the difference between MISR and MODIS aerosol optical depth retrievals over  
1600 mainland Southeast Asia, *Remote Sensing of Environment*, 113, 1-9,  
1601 <https://doi.org/10.1016/j.rse.2008.07.011>, 2009.

1602 Xie, Y., Li, Z., Zhang, Y., Zhang, Y., Li, D., Li, K., Xu, H., Zhang, Y., Wang, Y., and Chen, X.:  
1603 Estimation of atmospheric aerosol composition from ground-based remote sensing  
1604 measurements of Sun-sky radiometer, *J. Geophys. Res.- Atmos.*, 122, 498-518,  
1605 <https://doi.org/10.1002/2016JD025839>, 2017.

1606 Yang, S., Lau, W. K., Ji, Z., Dong, W., and Yang, S.: Impacts of radiative effect of pre-monsoon  
1607 biomass burning aerosols on atmospheric circulation and rainfall over Southeast Asia and  
1608 southern China, *Climate Dynamics*, 59, 417-432, <https://doi.org/10.1007/s00382-021-06135-7>,  
1609 2022.

1610 Yumul Jr, G. P., Cruz, N. A., Dimalanta, C. B., Servando, N. T., and Hilario, F. D.: The 2007 dry  
1611 spell in Luzon (Philippines): its cause, impact and corresponding response measures, *Climatic  
1612 change*, 100, 633-644, <https://doi.org/10.1007/s10584-009-9677-0>, 2010.

1613 Zhao, G., Di Girolamo, L., Dey, S., Jones, A. L., and Bull, M.: Examination of direct cumulus  
1614 contamination on MISR-retrieved aerosol optical depth and angstrom coefficient over ocean,  
1615 *Geophysical Research Letters*, 36, <https://doi.org/10.1029/2009GL038549>, 2009.

1616 Zhao, G., Zhao, C., Kuang, Y., Bian, Y., Tao, J., Shen, C., and Yu, Y.: Calculating the aerosol  
1617 asymmetry factor based on measurements from the humidified nephelometer system, *Atmos.  
1618 Chem. Phys.*, 18, 9049-9060, <https://doi.org/10.5194/acp-18-9049-2018>, 2018.